

# Chapter 1 Introduction

## 1.1 Overview of Vacuum Microelectronics

### 1.1.1 History

Vacuum tubes have been gradually replaced by those tiny volume, low cost, better reliability, and more power efficient solid state devices. Vacuum tubes have great improvements on semiconductor manufacturing technology for the past decades, the vacuum microelectronic devices using the professional micro fabrication technology have been successfully fabricated and gave a new life to vacuum electronics. “Vacuum state” devices have a number of remarkable advantages with respect to the present “solid state” devices. For example, the saturation drift velocity is limited to less than  $3 \times 10^7$  cm/s in all semiconductor due to scattering mechanism whereas the saturation drift velocity in vacuum is limited theoretically to  $3 \times 10^{10}$  cm/s and practically to about  $6-9 \times 10^8$  cm/s [1.1]. Moreover, because there is no medium to be damaged, either temporarily or permanently radiation effect should be negligible in vacuum devices. Additionally, there is no medium

for electrons fly in the vacuum, so there is no lattice scattering or bulk carrier generation/recombination. Therefore, the vacuum microelectronic devices can suffer to 500°C or above as long as the structures of the vacuum devices do not destroyed [1.2]. Table 1-1 shows the comparison between vacuum microelectronic and semiconductor devices.

Recent development in vacuum microelectronics started in 1928, when R. H. Fowler and L. W. Nordheim published the first theory of electron field emission from metals using quantum mechanics [1.3]. This theory is contrary to thermionic emission, which metals have to be heated so that some of the electrons in metal gain enough thermal energy to overcome the metal/vacuum barrier; according to the Fowler-Nordheim theory, an applied electric field of approximately  $10^3$  V/m is needed for electrons to tunnel through the sufficiently narrow barrier [1.3]. To reach this high field at reasonable applied voltage, it is customary to machine the field emitters into protruding objects to take advantage of field enhancement. It was not until 1968 when C. A. Spindt came up with a fabrication method to create very small dimension metal cones that vacuum microelectronic triodes became possible [1.2]. Figure 1-1 is a schematic diagram of the triode fabricated by Spindt. From the late 1960s to the year 1990, Ivor Brodie, Henry F. Gray,

and C. A. Spindt made many contributions to this field. Also, most of research was focused on the devices similar to the Spindt cathode during the past three decades.

In 1991, a group of research of the French company LETI CHEN reported a microtip display at the fourth International Vacuum Microelectronics Conference [1.4]. Their display was the first announcement of a practical vacuum microelectronic device. From then on, a great amount of researchers all over the world devoted themselves to this interesting, challenging, and inventive field. Part of the work focused on fabricating very small radius silicon tip by utilizing modern VLSI technology [1.5-1.6]. Some of them increased the emission current by coating different metals, such as W, Mo, Ta, Pt etc., even diamond on field emission arrays [1.7-1.9]. Then, in the past 30 years, field emission cold cathode materials became a promising technology and hundreds of research organizations devoted their money and innovation to its field emission application.

### **1.1.2 Applications of Vacuum Microelectronics**

Due to the superior properties of vacuum microelectronic devices, potential applications include high efficiency microwave amplifier and

generator [1.10-1.12]. ultra-fast computer, scanning electron microscopy, electron/ion source [1.13-1.14], micro-sensor, scanning electron microscopy, electron beam lithography, [1.15-1.16], temperature insensitive electronics, radiation hardness analog, and high brightness field emission flat-panel display [1.17-1.20].

Among these applications of the vacuum microelectronics, the first commercial product could be the field emission flat-panel display. The field emission fluorescent display is basically a thin cathode ray tube (CRT), which was first proposed by SRI International and later demonstrated by LETI [1.21].

Various kinds of flat-panel displays, such as liquid crystal display (LCD), light emitting display (LED), vacuum fluorescent display (VFD), plasma display panel (PDP), and electroluminescent display (EL), They all were developed for the better characteristics of small volume, light weight, and low power consumption. LCDs have become the most popular flat panel displays. However, LCDs have some drawbacks, such as poor viewing angle, temperature sensitivity and low brightness. As a result, some opportunities still exist and waiting for the solutions from other flat panel displays such as field emission display (FED).

### 1.1.3 Field Emission Displays

FED features all the pros of the CRTs in image quality and is flat and small volume. The schematic comparisons are revealed in Fig. 1-2. The operation of CRTs involves deflection of the beam in such a way that the electron spot scans the screen line-by-line. In FEDs, multiple electron beams are generated from the field emission cathode and no scanning of beams is required. The cathode is a part of the panel substrate consists of an X-Y electrically addressable matrix of field emission arrays (FEAs). Each FEA is located at the intersection of a row and a column conductor, with the row conductor serving as the gate electrode and the column conductor as the emitter base. The locations where the rows and columns intersect define a pixel. The pixel area and number of tips are determined by the desired resolution and luminance of the display. General, each pixel contains an FEA of 4-5000 tips. The emission current required for a pixel varies from 0.1 to 10  $\mu\text{A}$ , depending on the factors such as the luminance of the display, phosphor efficiency and the anode voltage. Compared to the active matrix LCDs, FEDs generate three times the brightness with wider viewing angle at the same power level. Full color FEDs have been developed by various research groups from different aspects such as PixTech, Futaba, Fujitsu,

Samsung, are presently engaged in commercially exploiting FED.

## 1.2 Materials and Structures of Cathode for Field Emission Displays

### 1.2.1 Theory Background

Electron field emission is a quantum mechanical tunneling phenomenon of electrons extracted from the conductive solid surface, such as a metal or a semiconductor, where the surface electric field is extremely high. If a sufficient electric field is applied on the emitter surface, electrons will be emitted through the surface potential barrier into vacuum, even under a very low temperature. In contrast, thermionic emission is the hot electron emission under high temperature and low electric field. Figure 1-3(a) demonstrates the band diagram of a metal-vacuum system.

Here  $W_0$  is the energy difference between an electron at rest outside the metal and an electron at rest inside the metal, whereas  $W_f$  is the energy difference between the Fermi level and the bottom of the conduction band. The work function  $\phi$  is defined as  $\phi = W_0 - W_f$ . If an external bias is applied, vacuum energy level is reduced and the potential barrier at the surface

becomes thinner as shown in Fig. 1-3(b). Then, an electron having energy “W” has a finite probability of passing through the surface barrier. Fowler and Nordheim derive the famous F-N equation (1.1) as follow [1.3]:

$$J = \frac{aE^2}{\phi^2(y)} \exp[-b\phi^{\frac{3}{2}}v(y)/E], \quad (1-1)$$

where J is the current density (A/cm<sup>2</sup>). E is the applied electric field (V/cm),  $\phi$  is the work function (in eV),  $a = 1.56 \times 10^{-6}$ ,  $b = -6.831 \times 10^{-7}$ ,  $y = 3.79 \times 10^{-4} \times 10^{-4} E^{1/2} / \phi$ ,  $t^2(y) \sim 1.1$  and  $v(y)$  can be approximated as [1.22]

$$v(y) = \cos(0.5\pi y), \quad (1-2)$$

or

$$v(y) = 0.95 - y^2, \quad (1-3)$$

Typically, the field emission current I is measured as a function of the applied voltage V. Substituting relationships of  $J = I/\alpha$  and  $E = \beta V$  into Eq.(1-1), where  $\alpha$  is the emitting area and  $\beta$  is the local field enhancement factor at the emitting surface, the following equation can be obtained

$$I = \frac{A\alpha\beta^2V^2}{\phi^2(y)} \exp[-bv(y)\frac{\phi^{\frac{3}{2}}}{\beta V}], \quad (1-4)$$

Then taking the log. form of Eq. (1-4) and  $v(y) \sim 1$

$$\log\left(\frac{I}{V^2}\right) = \log\left[1.54 \times 10^{-6} \frac{\alpha \beta^2}{\phi^2(y)}\right] - 2.97 \times 10^7 \left(\frac{\phi^{3/2} v(y)}{\beta V}\right), \quad (1-5)$$

from Eq. (1-5), the slope of a Fowler-Nordheim (F-N) plot is given by

$$S \equiv slope_{FN} = -2.97 \times 10^7 \left(\frac{\phi^2}{\beta}\right), \quad (1-6)$$

The parameter  $\beta$  can be evaluated from the slope  $S$  of the measured F-N plot if the work function  $\phi$  was known

$$\beta = -2.97 \times 10^7 \left(\frac{\phi^2}{S}\right) (cm^{-1}), \quad (1-7)$$

The emission area  $\alpha$  can be subsequently extracted from a rearrangement of Eq. (1-5)

$$\alpha = \left(\frac{I}{V^2}\right) \frac{\phi}{1.4 \times 10^{-6} \beta^2} \exp\left(\frac{-9.89}{\sqrt{\phi}}\right) \exp\left(\frac{6.53 \times 10^7 \phi^2}{\beta V}\right) (cm^2), \quad (1-8)$$

For example, the electric field at the surface of a spherical emitter of radius  $r$  concentric with a spherical anode (or gate) of radius  $r+d$  can be represented analytically by

$$E = \frac{V}{r} \left(\frac{r+d}{d}\right), \quad (1-9)$$

Though a realistic electric field in the emitter tip is more complicated than above equation, we can multiple Eq.(1-9) by a geometric factor  $\beta'$  to approximate the real condition.



$$E_{tip} \equiv \text{function of } (r, d) = \beta' \frac{V}{r} \left( \frac{r+d}{d} \right), \quad (1-10)$$

where  $r$  is the tip radius of emitter tip,  $d$  is the emitter-anode(gate) distance and  $\beta'$  is a geometric correction factor [1.23].

For a very sharp conical tip emitter, where  $d \gg r$ ,  $E_{tip}$  approaches to  $\beta'(V/r)$ . And for  $r \gg d$ ,  $E_{tip}$  approaches to  $\beta'(V/d)$  which is the solution for a parallel-plate capacitor and for a diode operation in a small anode-to-cathode spacing. As the gated FEA with very sharp tip radius, Eq. (1-10) can be approximated as:

$$E_{tip} = \beta'(V/r), \quad (1-11)$$

Combining  $E = \beta V$  and Eq. (1-11), we can obtain the relationship:

$$E_{tip} = \beta V = \beta'(V/r), \text{ and } \beta' = \beta r, \quad (1-12)$$

The tip radius  $r$  is usually in the range from a few nm to 50 nm, corresponding to the parameter  $\beta'$  ranging from  $10^{-1}$  to  $10^{-2}$ .

Besides, transconductance  $g_m$  of a field emission device is defined as the change in anode current due to a change in gate voltage [1.1].

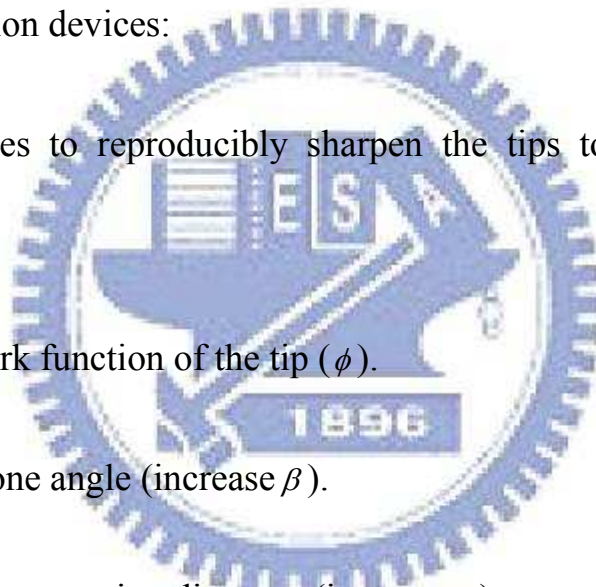
$$g_m = \left. \frac{\partial I_c}{\partial V_g} \right| V_c, \quad (1-13)$$

Transconductance of a FED is a figure of merit that gives as an

indication of the amount of current charge that can be accomplish by a given change in grid voltage. The transconductance can be increase by using multiple tips or by decreasing the gate-to-cathode spacing for a given anode-to-cathode spacing.

According to the above mention equations (especially Eq.1-5), the following approaches may therefore be taken to reduce the operating voltage of the field emission devices:

- 1) Find techniques to reproducibly sharpen the tips to the atomic level (increase  $\beta$ ).
- 2) Lower the work function of the tip ( $\phi$ ).
- 3) Narrow the cone angle (increase  $\beta$ ).
- 4) Reduce the gate-opening diameter (increase  $\beta$ ).



### 1.2.2 Spindt-type Field Emission

In 1968, the “Spindt” cathode was first proposed by C. A. [1.24]. The scanning electron microscope (SEM) image of a spindt type field emission triode has been shown in Fig. 1-1. It was first invented by Spindt of SRI and improved for the electron source of high-speed switching devices or

microwave devices [1.2]. Meyer of LETI presented the capability of using Spindt-type emitters for a display in 1970s [1.25] and stabilized the field emission from Spindt-type emitters by introducing a resistive layer as the feedback resistance.

The merits of the Spindt type field emitters are summarized as following: (1) High emission current efficiency, more than 98% anode current to cathode current can be achieved for the symmetric structure of Spindt tip and the gate hole, the lateral electric field to the metal tip can be cancelled out. (2) The fabrication is self-aligned, easy process; uniform field emission arrays can be fabricated easily. Some research groups have successfully fabricated commercial FED products based on Spindt type field emitters such as motorola, Pixtech, Futaba and Sony/Candesent.[1.26], the products of above mentioned companies are shown in Fig. 1-4.

However, there are some faults of Spindt-type field emitters when fabricating Spindt-type FED such as (1) High gate driving voltage required; for a Spindt-type field emission triode with 4  $\mu\text{m}$  gate aperture, the driving voltage is typically more than 60 V, which results in the high cost of the driving circuits. To reduce the gate driving voltage, frontier lithography technologies such as E beam lithography must be applied to reduce the gate

aperture to the sub-micron level. (2) The emission property degrades for the chemically instable of the metal tips. (3) Huge, expensive high vacuum deposition system required during fabricating large area Spindt-type FED.

### 1.2.3 BSD Field Emission

Panasonic and Tokyo University of Agriculture and Technology developed BSD(Ballistic Electron Surface Emitting Device). Figure 1-5 showed the operation diagram of BSD. The PPS (porous poly-Si) of cathodes of BSD have micro-crystal particles, which have a thin oxide film on itself. The offset voltages are applied between the anode and cathode, the electrons emitted by the cathode inject into the PPS, the electrons accelerated by the PPS interactions gain high energies and emit, and the emission efficiency of electrons is about 2%. Because the external voltages are focused on the oxide surface of the micro-crystal particles, then the thin film surface forms strong electrical fields, and the electrons can be emitted. However, the phenomenon called “Ballistic Electron Conduction”. In addition, the high active electrons are emitted from the cathode in the vertical direction without the deviation adjustment. The BSD has the advantages, such as simple structures, but it is very sensitive to the ion bombardments and has serious

drawbacks like the poor emission efficiency.

#### **1.2.4 MIM Field Emission**

MIM (Metal Insulator Metal) technology was investigated by Hitachi and LGE, but they didn't publish the detailed technology researches. According to the paper survey, MIM technology is the hot electron generation in the dielectric. The features of MIM are the low degrees of electron dispersion, low driving voltages, and high current density, but it is easily affected by the ion bombardments. However, the structure and fabrication of MIM are very complicated.

#### **1.2.5 Carbon and Nano-sized Field Emission**

The carbon nanotubes have their own advantageous properties, for example, the high aspect ratios, small tip radius of curvature, high Young's modulus, capability for the storage of a large amount of hydrogen, and structural diversities that make it possible for band gap engineering. These useful properties of carbon nanotubes (CNTs) make themselves good candidates for various applications, for instance, wires for nanosized electronic devices, super strong cables, AFM tips, charge-storage devices in

battery, and field emission display.

### **1.2.6 Surface Conduction Electron Emission (SCE)**

Canon and Toshiba created a new type of flat-panel display technology. Like conventional CRTs, SEDs utilize the collision of electrons with a phosphor-coated screen to emit light. The key technology to the electron emitters begins with the creation of an extremely narrow slits (~ several nanometers) between two electric poles in thin film of PdO (Palladium Oxide). Electrons are emitted from one side of the slit when approximately 10 V of electricity are applied. Some of these electrons are scattered at the other side of the slit and accelerated by the voltage (approximately 10 kV) applied between the glass substrates; causing light to be emitted when they collide with the phosphor-coated glass plate. The PdO film is coated by inject printing or screen-printing technology and this is a low cost process. The major problem of SED is that the efficiency is still low and the power consumption will be very high. Figure 1-6 shows the SEM image of SCE cathode array, structure and a 36-inch display of SED [1.27-1.28].

### **1.3 Synthesis Methods and Field Emission Properties of**

## **Carbon Nanotubes**

### **1.3.1 Structure of Carbon Nanotubes**

Carbon nanotubes are cylindrical molecules consisting of single or multi-graphite layers. Unlike other covalent matters, carbon shows various structures. The common allotropes of carbon are (1) graphite, (2) diamond, and (3) fullerene (Fig. 1-6). Among them, graphite is a planar structure of carbon in  $sp^2$  bonding. As the scale of graphite is close to the nano scale, it could curl and form a hollow tube. According to the number of layers in the tube wall, we classify the carbon nanotubes into two kinds: (1) single-walled (SWNTs) and (2) multi-walled carbon nanotubes (MWNTs) (Fig. 1-7).

#### **Single-walled Carbon Nanotubes**

The curling direction of graphite decides the characteristics of single-walled carbon nanotubes, like metal or semiconductor. Based on the curling direction, we can classify SWNTs into three kinds: (1) armchair, (2) zigzag, (3) chiral. The armchair SWNTs reveal metallic property. The zigzag and chiral SWNTs possess both of metallic and semiconductor properties.

#### **Multi-walled Carbon Nanotubes**

Since the distance between layers in MWNTs must satisfy 0.34nm, the curl direction of every layer may be different. MWNTs present different morphology by various growing parameters. In terms of appearance, we can approximately categorize MWNTs into several types: (1) standard tube, (2) spiral, and (3) “Y” model. If we further investigate the microstructure of the MWNTs, we can observe that there are different structures such as hollow-liked, bamboo-liked and fish-bone-liked MWNTs.

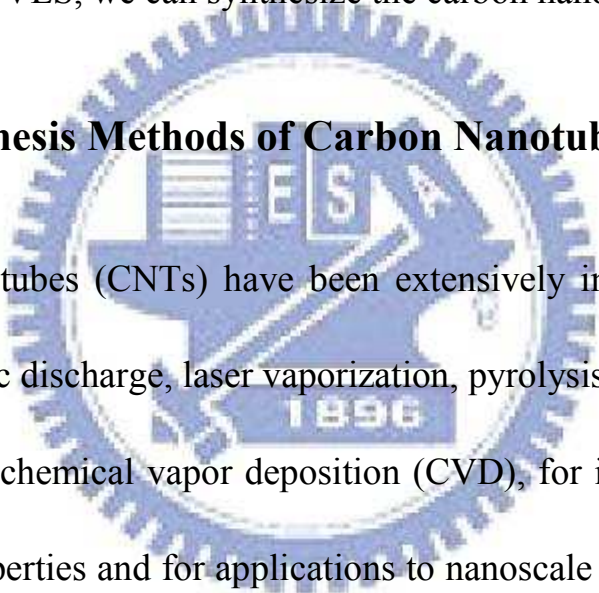
### **1.3.2 Physical and Chemical Properties of Carbon Nanotubes**

Carbon nanotubes have several superior characteristics, such as high thermal conductivity (2000 W/m.K), good heat resistance, low chemical reactivity, and high aspect ratio [1.29]. These properties are suitable for a field-emission source. In addition, carbon nanotubes have an excellent mechanical property, especially for the high Young modulus about 1.25T Pa [1.30]. But, CNTs have drawbacks, such as semiconductor/metal types [1.31], and uniformity growth issues. As the Fig. 1-8, carbon nanotubes growth can be classified into two types: tip growth model and base growth model. There are many explanations about carbon nanotubes growth mechanism. Generally speaking, the growth mechanism is VLS (Vapor



Liquid Solid). First, catalyst films transform to the particles because of thermal force or plasma. Formation of catalyst particles enhances the diffusion of carbon in the metal alloy. Second, the hydrocarbon precursors are decomposed from the reaction gases and carbon sources dissolve into the catalyst particles until the carbon saturation. Finally, carbons diffuse from the catalyst center to its surface and precipitate to form carbon SP<sup>2</sup> bonding. Then, through the VLS, we can synthesize the carbon nanotubes.

### **1.3.3 The Synthesis Methods of Carbon Nanotubes**



Carbon nanotubes (CNTs) have been extensively investigated for the synthesis using arc discharge, laser vaporization, pyrolysis, solar energy, and plasma-enhanced chemical vapor deposition (CVD), for its unique physical and chemical properties and for applications to nanoscale devices. However, common methods of CNT synthesis include: (1) arc-discharge [1.32], (2) laser ablation [1.33], (3) thermal CVD [1.34-1.36], and (4) plasma enhanced CVD [1.37-1.38].

The laser ablation can synthesize pure carbon nanotubes in high fabrication temperature, but large scale display panel can not be fabricated in the high fabrication temperature above the melting point of glass substrate.

The arc discharge can synthesize carbon nanotubes in shorter fabrication times, but it has some issues, such as (1) poor purity, (2) hard to control growth orientations of carbon nanotubes, and (3) poor emission uniformity. Compared to laser ablation and arc discharge, using CVD for carbon nanotube growth has some features, such as (1) high purity carbon nanotubes, (2) selective growth only for catalyst metal, (3) controlling growth direction, and (4) much suitable to semiconductor fabrication procedure. However, with the display technology trend, it is the time for large panel display. We need to synthesize carbon nanotubes using CVDs on large panel substrates. For this reason, carbon nanotube growth at low temperatures is unavoidable, but the purity of carbon nanotubes at low temperatures is poor. So, we still try some methods to increase growth rates at low temperatures, such as (1) multilayer catalysts, (2) plasma CVD, (3) post-treatment, and so on.

#### **1.3.4 Potential Application of Carbon Nanotube**

Since the discovery of CNTs in 1991, CNTs had attracted much attention for their unique physical and chemical properties. Their extensively potential applications lead them to become a super star of nano technology,

which cover: (1) Chemical sensor [1.39], (2) IR detector, (3) Nano-conducting Wire, (4) Vehicles for Hydrogen Storage [1.40], (5) Field Effect Transistor [1.41], (6) Field Emission Display (FED), (7) Probe of AFM and etc.

In the wide-ranging applications of CNTs, FED arouses researchers' interest particularly. In virtue of the superior field emission characteristics, CNTs are applied to the emitting source of cold cathode. The advantages of FED are its low response time, wide view angle, high brightness, high working temperature range and well combination with mature phosphor technology. However, a major problem needs to be solved in this field. It is not allowed to effectively analyze CNTs on a flat panel at relatively lower temperature ( $<500^{\circ}\text{C}$ ) and this barrier restriction obstructs the development of CNT-FED so far.

## **1.4 Thesis Organization**

The overview of vacuum microelectronics, field emission display and basic principles of field emission theory was described in chapter 1.

The experimental procedures were revealed in chapter 2. First, we utilize three types of bi-layered thin film, such as Ti-Ni, Ti-Fe and Ti-Co

catalysts then use them on silicon substrate to compare their morphology. Then, Use the same area but different array's edges to find the relation. Finally, we discussed the effect of R/H ratios of CNTs pillars. In the part, we investigated and found the relations of R/H ratios (inter-pillar spacing (R)/pillar height (H) ratios) to obtain the optimization and perimeter of the field emission characteristics.

Results and discussion were summarized in chapter 3. then, we accomplished many important results including, (1) SEM images, (2) TEM images, (3) AFM images, (4) Raman analysis, (5) EDS analysis, (6) XRD analysis, and (7) Field Emission Measurement.

Finally, the conclusions and future study are provided in chapter 4.

# Chapter 2 Experimental Procedures

## 2.1 Motivation

Some critical issues such as screening effects, reliability, high driving voltage, uniformity, and vacuum package have not been solved for the application of field emission displays. The effect of screening electric field by the dense arrangement of CNTs has been reported by several groups [2.1-2.3]. If the CNTs are too closely spaced, the electric field will be screened out. Groning et al. reported the field enhancement factor of the tips decreases rapidly when the inter-tip spacing is smaller than twice the length of the tips. They also found that the maximum current density is obtained when the spacing between the tips is about two times their relative height by simulations, as shown in Fig. 2-2. For larger spacing the current density decreases due to the decreasing the field emission sites, with a nearly constant emission current per tip as the field enhancement factor remains constant. The simulation of the equipotential lines of the electrostatic field for tubes are 1  $\mu\text{m}$  height and 2 nm radius, for distances between tubes of 4, 1, and 0.5  $\mu\text{m}$ . For smaller spacing the current density decreases rapidly due

to the decreasing factor and this effect cannot be compensated for by increasing the field emission sites from tips. This shows that when the spacing between the emitting structures on a surface becomes comparable to its length, problems of shielding do occur and will limit the emission current density.

Therefore, the turn-on field of the high-density-CNTs is still high because of the screening effects, as shown in Fig. 2-3. To obtain better field emission properties, the density of CNTs should be optimized. However, the density of CNTs synthesized by thermal CVD is too high and the screening effects are very serious. Many researches have reported different methods to suppress this phenomenon, such as plasma treatment [2.4-2.7], wet etching method [2.8], screen-printing method used pastes with different CNT contents [2.9-2.10], E-beam lithography [2.11-2.12], anodic aluminum oxide (AAO) nanoporous templates [2.13-2.14], excimer laser irradiation [2.15], and etc,. Most of the methods will increase the complexity in processes of fabrication or cause a defective affection on the CNTs.

In this chapter, we synthesize aligned CNTs pillar with each pillar composed of about a number density of  $10^{10} \text{ cm}^{-2}$ . Carbon nanotubes on the periphery of the pillar effect a dominant electric field concentration on their

tops and act as a major emission sites. Therefore, we treat each as a single field emitter and propose CNTs' pillar arrays as the field emitters to reduce the density of CNTs. The above idea is not only an effective way to reduce the complexity in processes but also a cost effective way to reduce the cost.

Besides, It has been reported that field emission can be effectively enhanced for aligned CNTs as field emitters when the ratio of distance between neighboring nanotubes ( $R$ ) to the height of each individual CNT ( $H$ ) is about 2[2.9]. Therefore, we try to use several bi-layered catalysts and change of growth parameters to find the most fitting one for pillar arrays' synthesis. Then, we study the effect of different pillar arrays' edges on the field emission characteristic using Co/Ti catalyst. Finally, we design and analyze the effect of  $R/H$  ratios with different inter-pillar distances on the field emission characteristics. The experiment procedures are shown in Fig. 2-1.

## **2.2 Growth of Carbon Nanotubes Pillar Arrays Using Ni/Ti, Fe/Ti and Co/Ti Bi-Layered Catalysts**

### **2.2.1 Forward Arrangement**

A (100) n-type silicon wafer is prepared for the substrate. After the RCA clean and lithography processes, we define three kinds of patterns for CNT field emission arrays. A 50-nm-thick Ti layer was deposited using a dual E-gun evaporation (JAPAN ULVAC EBX-10C) as a buffer layer between the catalyst and the substrate. Then three kinds of bi-layered catalysts are prepared by depositing Ni, Fe and Co with 5nm thickness on Ti film by E-gun evaporation, respectively. Each of the three bi-layered catalytic films are deposited layer by layer at the deposition rate of 0.1A/s ~ 0.2A/s using E-gun evaporation system. After the deposition of the catalysts into the patterns as described above, the photoresist is lifted off in acetone solution. At last, the samples are already accomplished for CNT growth.

### **2.2.2 Experimental Procedures**

An array of squares is formed on the photoresist coated n-type silicon wafers by lithography for selectively grown CNTs. The squares in array have the dimension of  $1000 \times 1000 \mu\text{m}^2$ . Subsequently, a 50-nm-thick Ti is deposited by the dual electron-gun evaporation system as a buffer layer to improve adhesion between the catalyst and the substrates, and to avoid silicon carbide formation.



The bi-layered Ni/Ti catalytic films are pretreated at 700°C with H<sub>2</sub>/N<sub>2</sub> (100/500 sccm), H<sub>2</sub>/N<sub>2</sub> (300/500 sccm), and H<sub>2</sub>/N<sub>2</sub> (500/500 sccm) for 15 minutes, respectively. The pretreatment conditions of CNTs in the thermal CVD system are shown in Fig. 2-4.

After pretreatment of bi-layered catalyst, we grow CNT at 700°C for 15 minutes and 45 minutes with H<sub>2</sub>/N<sub>2</sub>/C<sub>2</sub>H<sub>4</sub> (100/500/20sccm), respectively. The growth condition of CNTs in the thermal CVD system is shown in Fig. 2-5. We grow CNTs at 700°C with different flow rates of carbon source (20 and 40sccm of C<sub>2</sub>H<sub>4</sub>, respectively). The growth condition of CNTs in the thermal CVD system is shown in Fig. 2-6.

## **2.3 Field Emission Characteristics with Different Arrays Edges**

### **2.3.1 Pixel Design**

We define three kinds of patterns for CNT field emission arrays. First, design of 50×50 array of square pillar, each 20×20 μm<sup>2</sup> and 80 μm inter-pillar distance. Second, design of 5×5 array of square pillar, each 200×200 μm<sup>2</sup> and 80 μm inter-pillar distance. Third, design of one square cell with area of 1000×1000 μm<sup>2</sup>. The length of perimeter ratios is 50:5:1 as

shown in Fig. 2-7.

### 2.3.2 CNTs Synthesis

The samples with different catalysts are transferred into a thermal CVD chamber (Fig. 2-8). First, the catalyst film must be pretreated to form nanoparticles in  $H_2/N_2$ . Then, the hydrocarbon gas source is added to synthesize CNTs. The whole experimental process is schematically in Fig. 2-9.

To synthesize CNTs, several experimental conditions are designed. In nine experiments, we grow CNTs with different growth parameters at 700 °C.

#### Experimental Conditions

- 1.pretreatment: $H_2/N_2$ (**100**/500)15min, growth: $H_2/N_2/C_2H_4$ (**100**/500/20)30min.
- 2.pretreatment: $H_2/N_2$ (**300**/500)15min, growth: $H_2/N_2/C_2H_4$ (**100**/500/20)30min.
- 3.pretreatment: $H_2/N_2$ (**500**/500)15min, growth: $H_2/N_2/C_2H_4$ (**100**/500/20)30min.
- 4.pretreatment: $H_2/N_2$ (**100**/500)15min, growth: $H_2/N_2/C_2H_4$ (**300**/500/20)30min.
- 5.pretreatment: $H_2/N_2$ (**300**/500)15min, growth: $H_2/N_2/C_2H_4$ (**300**/500/20)30min.

6.pretreatment:H<sub>2</sub>/N<sub>2</sub>(**500**/500)15min, growth:H<sub>2</sub>/N<sub>2</sub>/C<sub>2</sub>H<sub>4</sub>(**300**/500/20)30min.

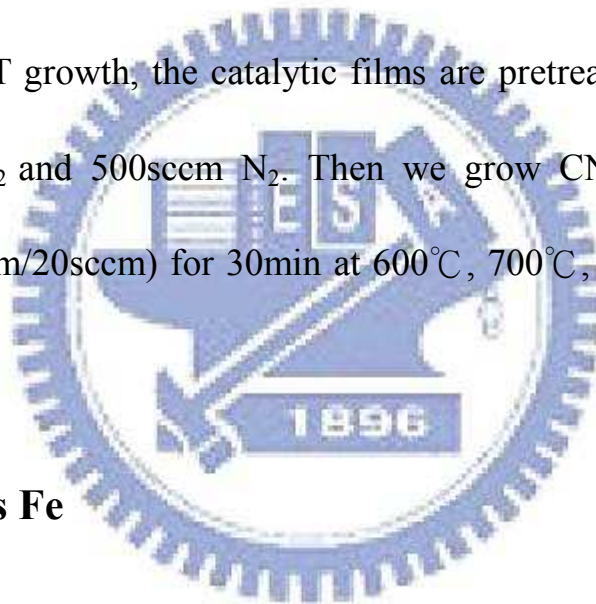
7.pretreatment:H<sub>2</sub>/N<sub>2</sub>(**100**/500)15min, growth:H<sub>2</sub>/N<sub>2</sub>/C<sub>2</sub>H<sub>4</sub>(**500**/500/20)30min.

8.pretreatment:H<sub>2</sub>/N<sub>2</sub>(**300**/500)15min, growth:H<sub>2</sub>/N<sub>2</sub>/C<sub>2</sub>H<sub>4</sub>(**500**/500/20)30min.

9.pretreatment:H<sub>2</sub>/N<sub>2</sub>(**500**/500)15min, growth:H<sub>2</sub>/N<sub>2</sub>/C<sub>2</sub>H<sub>4</sub>(**500**/500/20)30min.

### **2.3.3 Different Temperature**

Prior to CNT growth, the catalytic films are pretreated for 15 minutes with 300sccm H<sub>2</sub> and 500sccm N<sub>2</sub>. Then we grow CNTs in H<sub>2</sub>/N<sub>2</sub>/C<sub>2</sub>H<sub>4</sub> (500sccm/500sccm/20sccm) for 30min at 600°C, 700°C, 800°C, and 900°C, respectively.



### **2.3.4 Co versus Fe**

Prior to CNT growth, the Fe and Co catalytic films are pretreated at 700°C for 15 minutes with 300sccm H<sub>2</sub> and 500sccm N<sub>2</sub>. Then we grow CNTs for 30min with 20sccm C<sub>2</sub>H<sub>4</sub>, 500sccm H<sub>2</sub> and 500sccm N<sub>2</sub>.

The reliability of the pillar array is determined by a stress test at voltage of 650 V (4.33 V/μm) for one hour.

## **2.4 Field Emission Characteristics with Different Inter-Pillar**

## **Distances**

### **2.4.1 Inter-Pillar Distances Design**

We define three kinds of patterns for CNT field emission arrays. Design of 50×50 array of square pillar, each 20×20 μm<sup>2</sup>. First, the inter-pillar distance is 40 μm and the pixel area is 8.76×10<sup>6</sup> μm<sup>2</sup>. Second, the inter-pillar distance is 60 μm and the pixel area is 15.52×10<sup>6</sup> μm<sup>2</sup>. Third, the inter-pillar distance is 100 μm and the pixel area is 34.81×10<sup>6</sup> μm<sup>2</sup>. Design of the mask is shown in Fig. 2-10.

### **2.4.2 CNTs Synthesis**

Prior to CNT growth, the catalytic films are pretreated at 700°C for 15 minutes with 300sccm H<sub>2</sub> and 500sccm N<sub>2</sub>. Then we grow CNTs with 20sccm C<sub>2</sub>H<sub>4</sub>, 500sccm H<sub>2</sub> and 500sccm N<sub>2</sub>. The lengths of the CNT pillars synthesized for different times are about 12 μm for 15 minutes, 24 μm for 45 minutes, 35 μm for 60 minutes and 52 μm for 100 minutes, respectively.

## **2.5 Analysis**

Surface morphology and internal structure of CNTs synthesized in our

experiments are characterized by a Hitachi S-4700I high-resolution field-emission scanning electron microscopy (SEM) and JEOL, JEM-2100F high-resolution transmission electron microscopy (FE-TEM) respectively. In addition, A Raman spectrum is performed to offer the information about the crystallization of CNTs. The catalyst nanoparticles after pretreatment are analyzed by atomic force microscopy (AFM). The field emission properties of CNTs are characterized by a high – vacuum measurement environment with a base pressure of  $5 \times 10^{-6}$  Torr. Cathode contact was made directly on the wafer. A glass plate coated with indium-tin-oxide (ITO) was positioned 150  $\mu\text{m}$  above the tip of CNTs as an anode. All cables were shielded except for the ground return path to the power source. The emission current densities of CNTs were measured as a function of applied electron field, using Keithley 237 high voltage units as DC source and Keithley 238 high current units as ground source. The measurement was auto-controlled by the computer with IEEE 488 interface. The schematic experimental flow chart was shown in Fig. 2-11.

## Chapter 3 Results and Discussion

### 3.1 Growth of carbon nanotubes pillar arrays using Ni /Ti, Fe/Ti and Co/Ti bi-layered catalysts

Electron field emission from carbon nanotubes (CNTs) have attracted a great deal of intense academic and commercial interest since the first discovery of CNTs by Iijima in 1991[3.1], and is related to the fabrication of field emission displays. It is indispensable to reduce the turn on field and threshold field to achieve practically applicable field electron emitters that operate at lower power consumption. It has been reported that field emission can effectively enhanced for aligned CNTs as field emitters when the ratio of distance between neighboring nanotubes to the height of each individual CNT is about 2 [3.2]. However, the optimum rule ( $R/H=2$ ) for CNTs as electron field emitters has not been realized.

Carbon nanotubes (CNTs) on the periphery of each pillar can be envisioned as a major emission sites because of a dominant electric field concentration on their tops. Therefore, the above mentioned optimum rule seemed to be an interesting topic to enhance the field emission

characteristics for different ratio of inter-pillar distance (R) to pillar height (H). In this study, we regarded each pillar of CNTs as individual field emitter and tried to realize the optimal R/H ratio of 2 in order to obtain highly field emission enhancement. Therefore, the major work at present is to find the adequate catalyst and growth condition to grow aligned CNTs with uniform length.

### **3.1.1 Effect of H<sub>2</sub> pretreatment on Ni /Ti, Fe/Ti bi-layered catalysts**

It is generally believed that the diameter, growth rate, and density of carbon nanotubes (CNTs) could be controlled by the grain size and morphology of catalyst nanoparticles [3.3] which can be varied with the growth parameters of CVD, i.e., the H<sub>2</sub> flow rate and pretreatment time, thickness of catalyst film, composition of precursors, the growth temperature, etc. With decreasing the grain size of nanoparticles, the diameter of the nanotubes decreased, whereas the growth rate and density increased. Additionally, it has been reported that uniformly distributed catalytic nanoparticles with high density would contribute to the vertical alignment of CNTs at high growth temperature due to crowding effect [3.4]: the

confinement by neighboring nanotubes leads to a preferred growth direction perpendicular to the substrate. In this thesis, we tried to find out the field emission characteristics of pillar arrays of CNTs. The primary job is to find the growth conditions for the growth of pillar arrays of CNTs. We proceed to design some growth parameters of CVD. First, three kinds of catalyst are pre-treated with different flow rate of hydrogen gas for 15min at 700°C.

Figure 3-1 shows SEM and AFM micrographs of Ni /Ti bi-layered catalysts pre-treated in N<sub>2</sub>/H<sub>2</sub> gas mixtures with different hydrogen flow rates. The catalytic nanoparticles are distributed sparsely and some nanoparticles with larger sizes are also found. AFM micrograph also reveals the same results. The morphology of grown CNTs (not shown here) is curly due to the sparsely distributed catalytic nanoparticles.

Figure 3-2 shows SEM and AFM micrographs of Fe/Ti bi-layered catalysts pre-treated in N<sub>2</sub>/H<sub>2</sub> gas mixtures with different hydrogen flow rates. The SEM image in Fig. 3-2(a) shows that catalytic film are broken into large size, closely and uniformly distributed catalytic nanoparticles. The SEM image in Fig. 3-2(b) shows that catalytic film is pre-treated in 300scm H<sub>2</sub> gas. The catalytic film breaks into smaller nanoparticles with average sizes about 50nm in diameter when the H<sub>2</sub> flow rate is increased to 300scm.



Particle's size smaller than 25nm are distributed among the larger size particles. The SEM image in Fig. 3-2(c) shows that catalytic film is pre-treated in 500sccm H<sub>2</sub> gas. Large (about 40-50 nm) and small (about 10-20 nm) nanoparticles are uniformly distributed. It is not easy to get uniform size of nanoparticles for Fe/Ti bi-layered catalysts when we try to change other growth parameters of CVD.

Figure 3-3 is the typical SEM image using Fe/Ti bi-layered as catalysts for CNTs growth. It is observed from figure 3-3 that the CNTs produced are divided into two groups with the structure of the intermixture of long and short carbon nanotubes.

### **3.1.2 Effect of growth time on the morphology of CNTs grown by Fe/Ti bi-layered catalysts**

No matter how we change the pre-treatment time, pre-treatment temperature or hydrogen flow rate of pre-treatment, the growth condition to grow uniform length of carbon nanotubes is not easy to obtain. Finally, we fortunately find a growth condition to grow aligned CNTs with uniform length. The growth condition is described as below. When the temperature is stabilized at 700°C in pure N<sub>2</sub> gas, pre-treatment of 15 min with N<sub>2</sub>/H<sub>2</sub>

mixture gases (500sccm/100sccm) are fed into the furnace to pre-treat the catalytic film. Then, C<sub>2</sub>H<sub>4</sub> at 20sccm is added to the N<sub>2</sub>/H<sub>2</sub> mixture gases for CNTs' growth. The gas pressure is held at about 1atm and the growth time is 15 min. Figure 3-4(a) shows the SEM images of aligned CNTs with uniform length of about 12 μm. The growth condition looks like meet our requirement for pillar arrays of CNTs. However, the morphology of CNTs becomes non-uniform in length when we increase the growth time to 45min. Figure 3-4(b) shows the SEM images of aligned CNTs with 45min growth time. It is observed from the SEM image that the CNTs produced are divided into two groups. They are about 26 μm and 40 μm, respectively. Different height of uniform length of CNTs' pillar is needed because we want to study the field emission characteristics of carbon nanotubes pillar arrays for different ratios of inter-pillar distance (R) to pillar height (H). Therefore, increase of growth time in this growth condition to get different R/H ratios of CNTs' pillar is not the choice in our study.

### **3.1.3 Effect of carbon source flow rates on the morphology**

#### **of CNTs grown by Fe/Ti catalyst**

In order to obtain different R/H ratios of CNTS' pillar, we need to

grow different lengths of CNTs' pillar. Increasing growth time is not the right way to lengthen the CNTs' pillar height of uniform length. Now we try to change the flow rate of carbon source. We use the same growth condition as described in the section 3.1.2 except that the carbon source ( $C_2H_4$ ) is changed to 40sccm. Figure 3-5 shows the SEM image of CNTs grown with different flow rates of carbon source. The morphology of CNTs again appears two groups of different lengths (11.5  $\mu m$  and 20  $\mu m$ , respectively). Therefore, the attempt to lengthen the pillar height of uniform length is wrong.

We have tried all of the possible was to increase the pillar height of uniform length in order to get different R/H ratios. The choice of Fe/Ti bi-layered catalyst is probably not appropriate.

### **3.1.4 Effect of $H_2$ pretreatment on Co/Ti bi-layered catalysts**

Figure 3-6 shows SEM and AFM micrographs of Co/Ti bi-layered catalysts pre-treated in  $N_2/H_2$  gas mixtures with different hydrogen flow rates. The SEM images in Fig. 3-6 show that catalytic nanoparticles are distributed uniformly when Co/Ti bi-layered catalysts is pre-treated with different flow rates of hydrogen gas. Besides, the nanoparticle' size is very

uniform (about 15-25nm) and the density is very high ( $5 \times 10^{10}/\text{cm}^2$ ). The AFM images in Fig. 3-6 show that the nanoparticles' surface roughness of Co/Ti bi-layered catalysts with different flow rates of hydrogen gas pre-treatment is very low as compared to the other two bi-layered catalytic films (Ni/Ti and Fe/Ti).

As previous section described, uniformly distributed catalytic nanoparticles with high density would contribute to the vertical alignment of CNTs at high growth temperature due to crowding effect. Besides, several research groups [3.5-3.6] reported that the diameter of the catalyst nanoparticles tends to corresponding to the diameter of the multiwalled CNTs (MWNTs) for TCVD. Therefore, we predicts that CNTs grown by Co/Ti catalyst will probably be pillar with uniform length due to high density, uniform distribution and size of catalytic nanoparticles.

### **3.1.5 Effect of growth time on the morphology of CNTs grown by Co/Ti bi-layered catalysts**

We choose one of the pre-treatment conditions of Fig. 3.6 to grow carbon nanotubes pillar arrays. In fact, all of the conditions can grow CNTs pillar arrays and can easy to lengthen its length. The pre-treatment condition

we choose is as follows. Co/Ti bi-layered catalyst is pre-treated for 15 min in  $N_2/H_2$  mixture gases (500sccm/100sccm). Then,  $C_2H_4$  at 20sccm is added to the  $N_2/H_2$  mixture gases for CNTs' growth. The gas pressure is held at about 1atm and the growth time is 15 min and 45min, respectively. Figure 3.7 shows the SEM images of CNTs grown for different times. The length of CNTs is increased from 13.2  $\mu m$  to 51  $\mu m$  when the growth time is increased from 15 min to 45 min. The phenomenon of two groups of CNTs disappears.

### **3.1.6 Effect of growth temperature on the morphology of CNTs grown by Co/Ti bi-layered catalysts**

Figure 3-7 SEM micrographs of Co /Ti bi-layered catalysts pre-treated in  $N_2/H_2$  gas mixtures with different growth temperatures and their morphology of CNTs. The catalytic nanoparticles distribute uniformly, and the nanoparticle' size is very uniform and with high density when temperature is operated from 600°C to 800°C. The morphology of CNTs is vertically aligned and length control of carbon nanotubes' pillar arrays can be achieved by change the growth temperature. When the growth temperature is 900°C, the catalytic nanoparticles distribute non-uniformly

with low density and the range of particles' size becomes larger. Therefore, the morphology of CNTs grows curly and no longer be pillar arrays.

### **3.1.7 SEM and TEM micrographs' comparison of CNTs grown using (a) Co/Ti (b) Fe/Ti (c) Ni/Ti bi-layered catalyst**

Figure 3-9 shows the SEM and TEM micrograph of CNTs grown using (a) Co/Ti (b) Fe/Ti (c) Ni/Ti bi-layered catalyst. From the SEM images of Fig. 3.9(a) - (c), the CNTs grown are vertically aligned with uniform length, two vertically aligned groups with different lengths and curly distribution, respectively. CNTs grown by these three kinds of catalysts are multiwall with bamboo-like hollow structure. Well-structured graphite sheets parallel to the tube axis and catalytic particle existing at the tip of the tube are observed from the TEM images of Fig. 3.9(a) - (b). There are few well parallel graphite sheets and catalytic particles are found in the tube not at the tip or the bottom of the tubes.

## **3.2 The relation between field emission characteristics and perimeter of the field emission arrays**

The CNTs pillar is aligned perpendicular to the substrate surface and

consists of CNTs with a number density of  $10^{10} \text{ cm}^{-2}$ . Carbon nanotubes on the periphery of the pillar effect a dominant electric field concentration on their tops and act as a major emission sites. Therefore, the relation between field emission characteristics and perimeter of the field emission arrays is needed to study further.

### 3.2.1 Pixel design

We study the relation between field emission characteristics and perimeter of the field emission arrays with pixel design which are arrays of  $1 \times 1$  (each  $1000 \times 1000 \text{ } \mu\text{m}^2$ ),  $5 \times 5$  (each  $200 \times 200 \text{ } \mu\text{m}^2$ ) and  $50 \times 50$  (each  $20 \times 20 \text{ } \mu\text{m}^2$ ) square patterns, respectively. Figure 2-7 shows the pixel design in our mask. The above three pixel designs have the same field emission area ( $10^6 \text{ } \mu\text{m}^2$ ) and their perimeter ratio is 50:5:1.

Figure 3-11(a) shows the J-E and F-N plot for small, middle, and large sizes of CNTs' arrays. The corresponding F-N plots are shown in the inset of Fig. 3-11(a) and the linearity of these plots confirmed the field-emission phenomenon. Table3-1 shows that the turn-on field decreases from 2.067 to  $1.4 \text{ V}/\mu\text{m}$  and the field emission current density increases from 6.13 to  $309.4 \text{ mA}/\text{cm}^2$  at  $6.667 \text{ V}/\mu\text{m}$  for large, middle, and small sizes of CNTs' arrays.

The small size of CNTs' array (i.e. 50×50 square patterns and each 20×20 μm<sup>2</sup>) achieves the lowest turn-on field and the highest field emission current density at 6.667 V/μm among the three different sizes' design of CNTs arrays.

Carbon nanotubes on the periphery of the pillar act as a major emission sites the electron field emission can be neglected inside the pillar due to the field screening effect. Therefore, we speculate that the field emission current density has a strong relation to the perimeters of the field emission arrays. It is interesting for us to find that the ratio of field emission current density at 6.667 V/μm is about 66:7:1 which is proportional to the perimeters' ratio (50:5:1) for large, middle, and small sizes of CNTs' arrays. Further study is needed to find the real relation between them.

Finally, we choose pixel design with 50×50 square patterns and each 20×20 μm<sup>2</sup> to study the optimal R/H ratio of carbon nanptubes pillar arrays.

### **3.2.2 Optimal growth condition**

Table 3-2 shows the experimental design of CNTs synthetic conditions of finding the optimum growth condition. The experimental design of CNTs synthetic conditions are described as below. When the



temperature is stabilized at 700°C in pure N<sub>2</sub> gas, pre-treatment of 15 min with N<sub>2</sub>/H<sub>2</sub> mixture gases are fed into the furnace to pre-treat the catalytic film. In the pre-treatment process, N<sub>2</sub> is fixed at 500sccm and H<sub>2</sub> is fixed at 100, 300 and 500sccm, respectively. Then, C<sub>2</sub>H<sub>4</sub> at 20sccm is added to the N<sub>2</sub>/H<sub>2</sub> mixture gases for CNTs' growth. In the CNTs' growth, H<sub>2</sub> is fixed at 100, 300 and 500sccm, respectively. The gas pressure is held at about 1atm and the growth time is 30 min.

Figure 3-12 shows the SEM micrographs of CNTs synthetic conditions in our experimental design. The length of CNTs is decreased when H<sub>2</sub> is increased from 100sccm to 500sccm due to the content of carbon source is decreased from 20/620 to 20/1020. Besides, the CNTs pillar arrays are of uniform length for all of the synthetic conditions.

Figure 3-13 shows Raman and I-V plot in the experimental design of CNTs synthetic conditions. The Raman spectrum clearly shows two sharp peaks at approximately 1350 cm<sup>-1</sup> (D band) and 1580 cm<sup>-1</sup> (G band). The high intensity at approximately 1580 cm<sup>-1</sup> confirms that the CNTs have a highly crystalline graphite structure for all cases in the experimental design of CNTs synthetic conditions. Especially, in the pre-treatment case with N<sub>2</sub> is fixed at 500sccm and H<sub>2</sub> is fixed at 300sccm, the ratio of I<sub>g</sub>/I<sub>d</sub> is larger

than the other cases. Figure 3-13(b) shows I-V plot in the experimental design of CNTs synthetic conditions. The lower turn-on field and higher field emission current density at  $6.667 \text{ V}/\mu\text{m}$  is achieved in the synthetic conditions from case 4 to case 6. We attribute this better field emission phenomena is due to the higher crystalline graphite structure which is confirmed in the Raman spectrum.

Table 3-3 shows the summarized of turn-on field, threshold field and emission current density at  $6.67 \text{ V}/\mu\text{m}$  of CNTs between CNTs synthetic conditions in our experimental design.

### **3.2.3 Comparison of morphology and field emission characteristics of CNTs grown by Co catalyst with that by Fe catalyst**

Figure 3-14 shows morphology and field emission characteristics of CNTs Grown by Co and Fe Catalyst, respectively. Pillar arrays of CNTs with uniform length are achieved in Co catalyst and two groups of CNTs with different length is achieved in Fe catalyst. As discussed in the previous section, CNTs pillar arrays can achieve better field emission characteristics. However, two groups of CNTs with different length can also have better

field emission characteristics due to the separation between CNTs of each of the two groups is large. Therefore, the corresponding density of each part of CNTs is reduced and this structure of CNTs will be subject to less field screening from surrounding nanotubes. The turn-on fields of CNTs Grown by Co and Fe Catalyst is about the same ( $1.6 \text{ V}/\mu\text{m}$  for Co case and  $1.9 \text{ V}/\mu\text{m}$  for Fe case). The field emission current density at  $6.667 \text{ V}/\mu\text{m}$  achieve  $678.2 \text{ mA}/\text{cm}^2$  and  $730.7 \text{ mA}/\text{cm}^2$  for Co and Fe catalyst, respectively. Therefore, the above two morphologies of CNTs may meet the requirements for field emission display application.

Figure 3-15 and Table 3-4 show the field emission stability at 650V and emission image of CNTs grown by Co and CNTs grown by Fe. Better emission uniformity and stability is achieved in CNTs grown by Co catalyst.

### **3.3 Field emission characteristics with different R/H ratios**

Since CNTs pillar arrays has very well field emission properties, different ratios of inter-pillar distance (R) to pillar height (H) come out to be an important topic to achieved well field emission characteristics. In this section, different R/H ratios are designed by changing the inter-pillar distance and CNTs length.

### **3.3.1 Different R/H Ratios with 40 $\mu\text{m}$ Inter Pillar Distance**

We grow different CNTs lengths with 40  $\mu\text{m}$  inter pillar distance to get different R/H ratios. Figure 3-16 shows SEM micrograph for different R/H ratios with 40  $\mu\text{m}$  inter pillar distance. The R/H ratios are 3.48, 1.74, 1.116 and 0.787, respectively. Figure 3-17 shows field emission characteristics of different R/H Ratios with 40  $\mu\text{m}$  inter pillar distance. The turn on field is 2.79, 2.11, 2.98 and 4.14  $\text{V}/\mu\text{m}$ , respectively. The better field emission characteristic is achieved when the R/H ratio is close to 2.

### **3.3.2 Different R/H Ratios with 60 $\mu\text{m}$ Inter Pillar Distance**

We grow different CNTs lengths with 60  $\mu\text{m}$  inter pillar distance to get different R/H ratios. Figure 3-18 shows SEM micrograph for different R/H ratios with 60  $\mu\text{m}$  inter pillar distance. The R/H ratios are 5.83, 2.58, 1.75 and 1.145, respectively. Figure 3-19 shows field emission characteristics of different R/H Ratios with 40  $\mu\text{m}$  inter pillar distance. The turn on field is 2.27, 1.797, 1.71 and 4.14  $\text{V}/\mu\text{m}$ , respectively. The better field emission characteristic is achieved when the R/H ratio is close to 2.

### **3.3.3 Different R/H Ratios with 100 $\mu\text{m}$ Inter Pillar Distance**

We grow different CNTs lengths with 100  $\mu\text{m}$  inter pillar distance to get different R/H ratios. Figure 3-20 shows SEM micrograph for different R/H ratios with 100  $\mu\text{m}$  inter pillar distance. The R/H ratios are 9.9, 4.63, 3.145 and 2.041, respectively. Figure 3-21 shows field emission characteristics of different R/H Ratios with 40  $\mu\text{m}$  inter pillar distance. The turn on field is 2.267, 1.406, 1.197 and 0.808V/ $\mu\text{m}$ , respectively. The better field emission characteristic is achieved when the R/H ratio is close to 2.

### **3.4 Comparison of Experimental Results with Simulation Results to the Effect of R/H Ratios on Field Emission Current Density**

In this section, we try to use our data to compare experimental results with simulation results to the effect of R/H ratios on field emission current at 7.4 V/ $\mu\text{m}$ .

#### **3.4.1 Different R/H Ratios with CNTs' Length is Fixed at 10 $\mu\text{m}$**

We grow CNTs length of 10  $\mu\text{m}$  with different inter pillar distances to study the effect of R/H ratios on field emission current at fixed electric field.

Figure 3.22 shows SEM micrograph of different R/H ratios with CNTs' length is fixed at 10  $\mu\text{m}$ . The R/H ratios are 3.48, 5.83 and 9.9, respectively.

Figure 3.23 shows that field emission characteristics of different R/H ratios with CNTs' length fixed at 10  $\mu\text{m}$ . The field emission current density is 12.83, 9.38 and 8.64  $\text{mA}/\text{cm}^2$ , respectively.

### **3.4.2 Different R/H Ratios with CNTs' Length is Fixed at 34 $\mu\text{m}$**

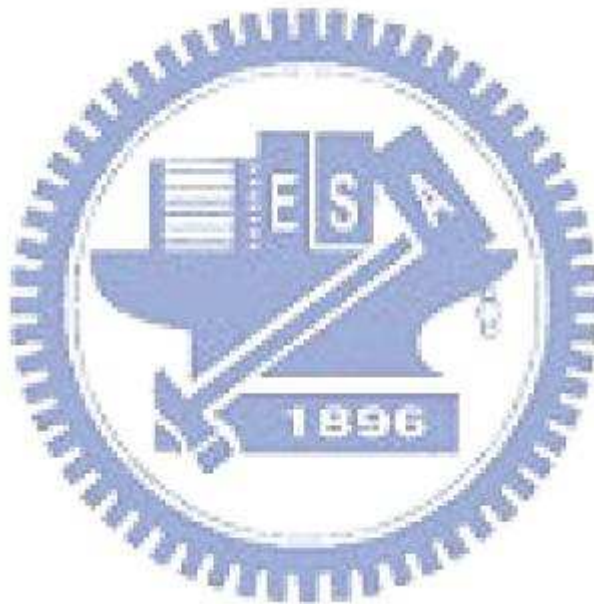
We grow CNTs length of 34  $\mu\text{m}$  with different inter pillar distances to study the effect of R/H ratios on field emission current at fixed electric field.

Figure 3.24 shows SEM micrograph of different R/H ratios with CNTs' length is fixed at 10  $\mu\text{m}$ . The R/H ratios are 1.166, 1.749 and 3.135, respectively. Figure 3.25 shows that field emission characteristics of different R/H ratios with CNTs' length fixed at 10  $\mu\text{m}$ . The field emission current density is 3.86, 17.26 and 15.17  $\text{mA}/\text{cm}^2$ , respectively.

### **3.4.3 Comparison Result between Experimental and Simulation Results**

Figure 3-26 Comparison of experimental results with simulation results

to the effect of R/H ratios on field emission current at  $7.4 \text{ V}/\mu\text{m}$ . The experimental results show that the experimental results are in accordance with the simulation results well.



# Chapter 4 Summary and Conclusions

## 4.1 Summary and Conclusions

It is indispensable to reduce the turn on field and threshold field to achieve practically applicable field electron emitters that operate at lower power consumption. It has been reported that field emission can effectively be enhanced for aligned CNTs as field emitters when the ratio of distance between neighboring nanotubes to the height of each individual CNT is about 2. Carbon nanotubes (CNTs) on the periphery of each pillar can be envisioned as a major emission site because of a dominant electric field concentration on their tops. Therefore, the above mentioned optimum rule seemed to be an interesting topic to enhance the field emission characteristics for different ratio of inter-pillar distance ( $R$ ) to pillar height ( $H$ ).

We use Ni/Ti, Fe/Ti and Co/Ti bi-layered catalysts to grow CNTs pillar arrays with uniform length and successfully to grow CNTs pillar arrays with uniform length by Co/Ti bi-layered catalysts. The Co nanoparticles are smaller, denser, and more uniform in size distribution than those for the



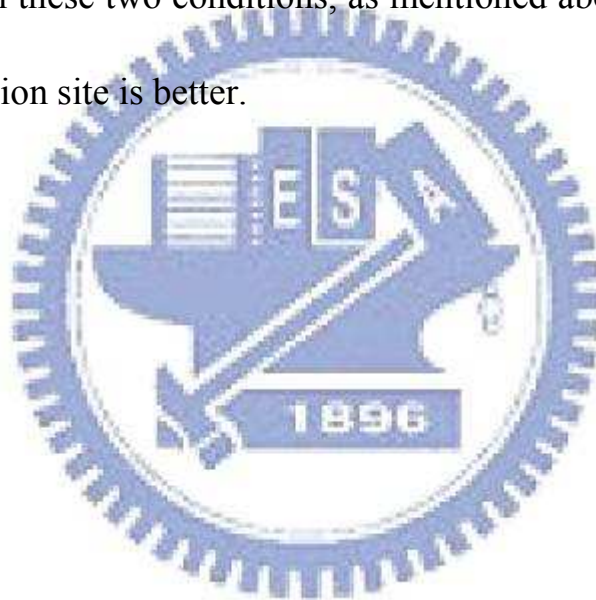
other two catalysts. Therefore, it leads to the uniformly grown longer CNT pillars with the CNTs smaller diameter. Whatever we change the growth parameters, it is very easy to grow CNTs pillar arrays with uniform length by Co/Ti bi-layered catalysts.

Carbon nanotubes at the edge of each pillar suffer less field screening effect, therefore, the field emission characteristics will probably tend to be strongly related to the total perimeters of the pixel. The ratio of the field emission current densities at  $6.667 \text{ V}/\mu\text{m}$  for small, middle, and large sizes of patterns is about  $66 : 7 : 1$ . Uniform length of CNT pillars can be achieved under the temperatures ranging from  $600 \text{ }^\circ\text{C}$  to  $800 \text{ }^\circ\text{C}$  via the Co/Ti catalyst. By the way, better uniformity of luminescent images can be also obtained.

Structure of CNTs pillar arrays with uniform length is proved to be a choice to achieved best field emission characteristics. Besides, we also find that optimum ratio of inter-pillar distance (R) to pillar height (H) for carbon nanotubes pillar arrays is also close 2.

To achieve the best field emission characteristics, the optimum design rule of pixel design is as follows:

1. R/H ratio = 2
2. Under the fulfillment of pillar type of CNTs, the size of each pillar should be as small as possible and the peripheral length should be as longer as possible.
3. Based on these two conditions, as mentioned above area, we hoped more emission site is better.



<b>Items</b>	<b>Solid State Microelectronics</b>	<b>Vacuum Microelectronics</b>
<b>Current Density</b>	<b><math>10^4 - 10^5</math> (A/cm<sup>2</sup>)</b>	<b>similar</b>
<b>Turn-on Voltage</b>	<b>0.1 – 0.7 V</b>	<b>5 – 300 V</b>
<b>Structure</b>	<b>solid/solid interface</b>	<b>solid/vacuum interface</b>
<b>Electron Transport</b>	<b>in solid</b>	<b>in vacuum</b>
<b>Electron Velocity</b>	<b><math>3 \times 10^7</math> (cm/sec)</b>	<b><math>3 \times 10^{10}</math> (cm/sec)</b>
<b>Flicker Noise</b>	<b>due to interface</b>	<b>due to emission</b>
<b>Thermal &amp; Short Noise</b>	<b>comparable</b>	<b>comparable</b>
<b>Electron Energy</b>	<b>&lt; 0.3 eV</b>	<b>a few to 1000 eV</b>
<b>Cut-off Frequency</b>	<b>&lt; 20 GHz (Si) &amp; 100 GHz (GaAs)</b>	<b>&lt; 100 – 1000 GHz</b>
<b>Power</b>	<b>small – medium</b>	<b>medium – large</b>
<b>Radiation Hardness</b>	<b>poor</b>	<b>excellent</b>
<b>Temperature Effect</b>	<b>-30 – 50 °C</b>	<b>&lt; 500 °C</b>
<b>Fabrication &amp; Materials</b>	<b>well established (Si) &amp; fairly well (GaAs)</b>	<b>not well established</b>

Table 1-1 Comparison between vacuum microelectronics and solid-state electronics.

Synthesis Condition	Turn-on field at 10 $\mu\text{A}/\text{cm}^2$	Threshold field at 10 $\text{mA}/\text{cm}^2$	Emission current density at 6.667 $\text{V}/\mu\text{m}$
Large	2.067 $\text{V}/\mu\text{m}$	N.A	6.13 $\text{mA}/\text{cm}^2$
Middle	1.733 $\text{V}/\mu\text{m}$	4.37 $\text{V}/\mu\text{m}$	44.07 $\text{mA}/\text{cm}^2$
Small	1.4 $\text{V}/\mu\text{m}$	3.8 $\text{V}/\mu\text{m}$	398.3 $\text{mA}/\text{cm}^2$



Table 3-1 Comparisons of turn-on field, threshold field and emission current density at 6.67V/ $\mu\text{m}$ s of CNTs between small, middle, and large sizes of pillar arrays.

Process Temp.	Synthesis Condition	Synthesis Diagram
700°C	<p><b>N<sub>2</sub>/H<sub>2</sub>, N<sub>2</sub>/H<sub>2</sub>/C<sub>2</sub>H<sub>4</sub></b></p> <p>1.500/100, 500/100/20</p> <p>2.500/100, 500/300/20</p> <p>3.500/100, 500/500/20</p> <p>4.500/300, 500/100/20</p> <p>5.500/300, 500/300/20</p> <p>6.500/300, 500/500/20</p> <p>7.500/500, 500/100/20</p> <p>8.500/500, 500/300/20</p> <p>9.500/500, 500/500/20</p>	<p>The synthesis diagram plots temperature in degrees Celsius against time in minutes. The temperature starts at 0°C, rises linearly to 700°C at 10 minutes, and then remains constant at 700°C until 55 minutes. A grey shaded area from 0 to 10 minutes is labeled 'Pretreatment Region'. Gas flow rates are indicated: N<sub>2</sub>=600sccm (0-10 min), N<sub>2</sub>=500sccm, H<sub>2</sub>=100sccm (10-25 min), and N<sub>2</sub>=500sccm, H<sub>2</sub>=100sccm, C<sub>2</sub>H<sub>4</sub>=20sccm (25-55 min).</p>

Table 3-2 Experimental design of CNTs synthetic conditions of finding the optimum growth condition

Synthesis Condition	Turn-on field at 10 $\mu\text{A}/\text{cm}^2$	Threshold field at 10 $\text{mA}/\text{cm}^2$	Emission current density at 6.667 $\text{V}/\mu\text{m}$
1.500/100,500/100/20	2.33 $\text{V}/\mu\text{m}$	4.067 $\text{V}/\mu\text{m}$	22.18 $\text{mA}/\text{cm}^2$
2.500/100,500/300/20	1.87 $\text{V}/\mu\text{m}$	3.733 $\text{V}/\mu\text{m}$	148.6 $\text{mA}/\text{cm}^2$
3.500/100,500/500/20	1.47 $\text{V}/\mu\text{m}$	3.8 $\text{V}/\mu\text{m}$	204.8 $\text{mA}/\text{cm}^2$
4.500/300,500/100/20	1.6 $\text{V}/\mu\text{m}$	3.933 $\text{V}/\mu\text{m}$	611.9 $\text{mA}/\text{cm}^2$
5.500/300,500/300/20	2.22 $\text{V}/\mu\text{m}$	3.8 $\text{V}/\mu\text{m}$	629.2 $\text{mA}/\text{cm}^2$
6.500/300,500/500/20	2.07 $\text{V}/\mu\text{m}$	3.789 $\text{V}/\mu\text{m}$	900.1 $\text{mA}/\text{cm}^2$
7.500/500,500/100/20	2.0 $\text{V}/\mu\text{m}$	3.652 $\text{V}/\mu\text{m}$	148.6 $\text{mA}/\text{cm}^2$
8.500/500,500/300/20	2.0 $\text{V}/\mu\text{m}$	3.8 $\text{V}/\mu\text{m}$	259.1 $\text{mA}/\text{cm}^2$
9.500/500,500/500/20	1.93 $\text{V}/\mu\text{m}$	3.8 $\text{V}/\mu\text{m}$	376.5 $\text{mA}/\text{cm}^2$



Table 3-3 Comparisons of turn-on field, threshold field and emission current density at 6.67V/ $\mu\text{m}$ s of CNTs between CNTs synthetic conditions in our experimental design

Catalyst	Stress Field Emission	Average Current Density	Fluctuation (%)
Co	4.33 V/ $\mu\text{m}$	18.4 mA/cm <sup>2</sup>	$\pm 6.52\%$
Fe	4.33 V/ $\mu\text{m}$	19.1 mA/cm <sup>2</sup>	$\pm 7.87\%$



Table 3-4 Comparison of field emission current fluctuation at 650V between CNTs grown by Co catalyst and CNTs grown by Fe catalyst

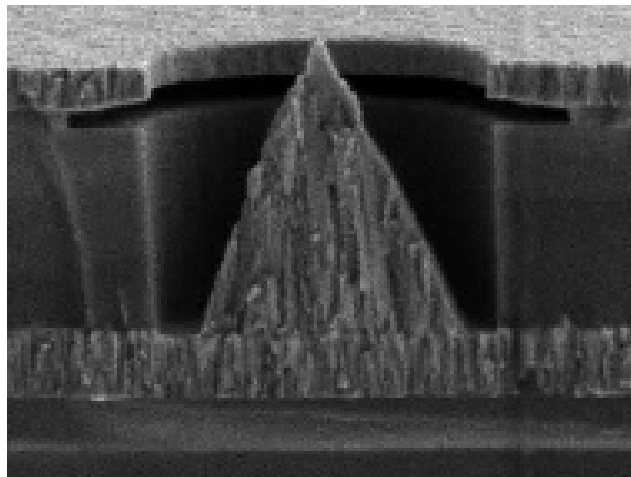
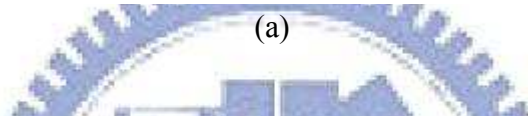
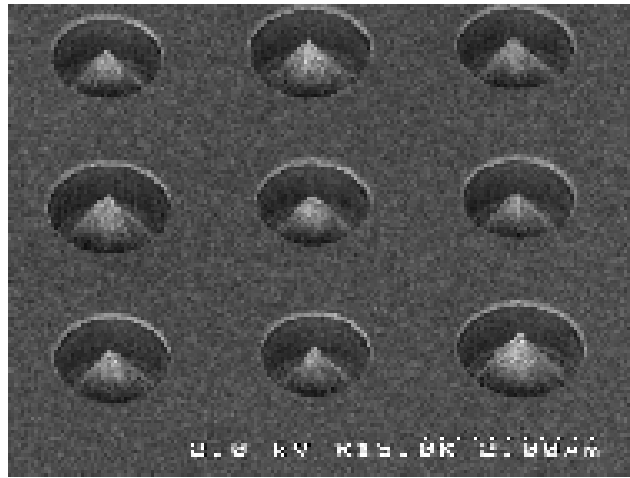
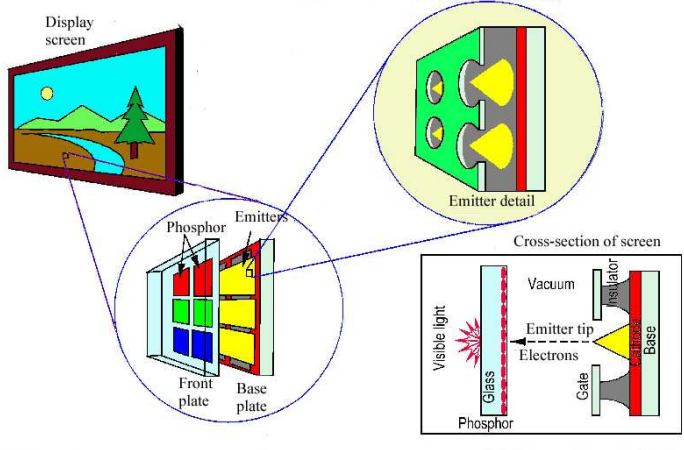
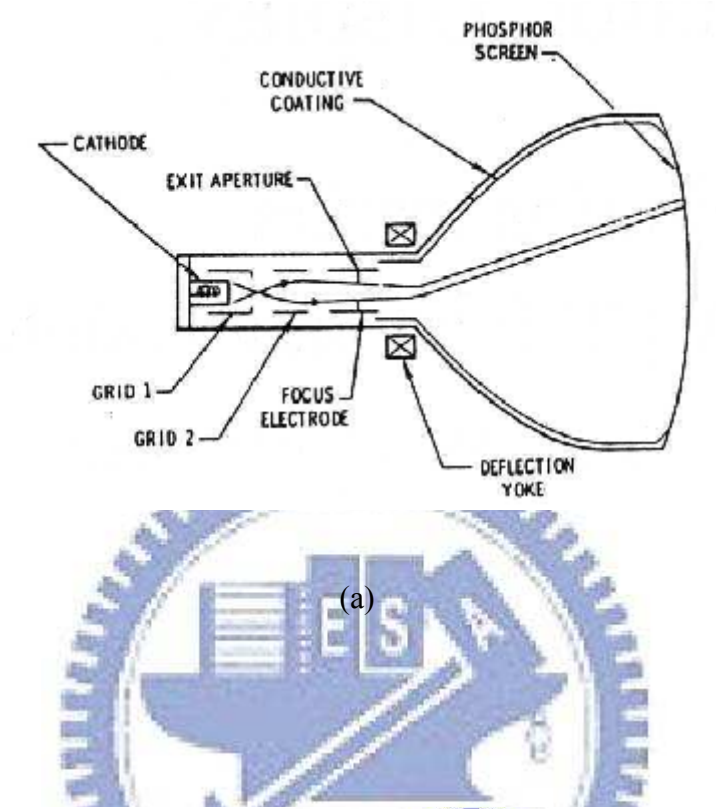


Figure 1-1 The SEM micrograph of (a) Spindt type triodes array, (b) Spindt type field emission triode





(b)

Figure 1-2 The schematic diagram of (a) conventional CRT, (b) FED.

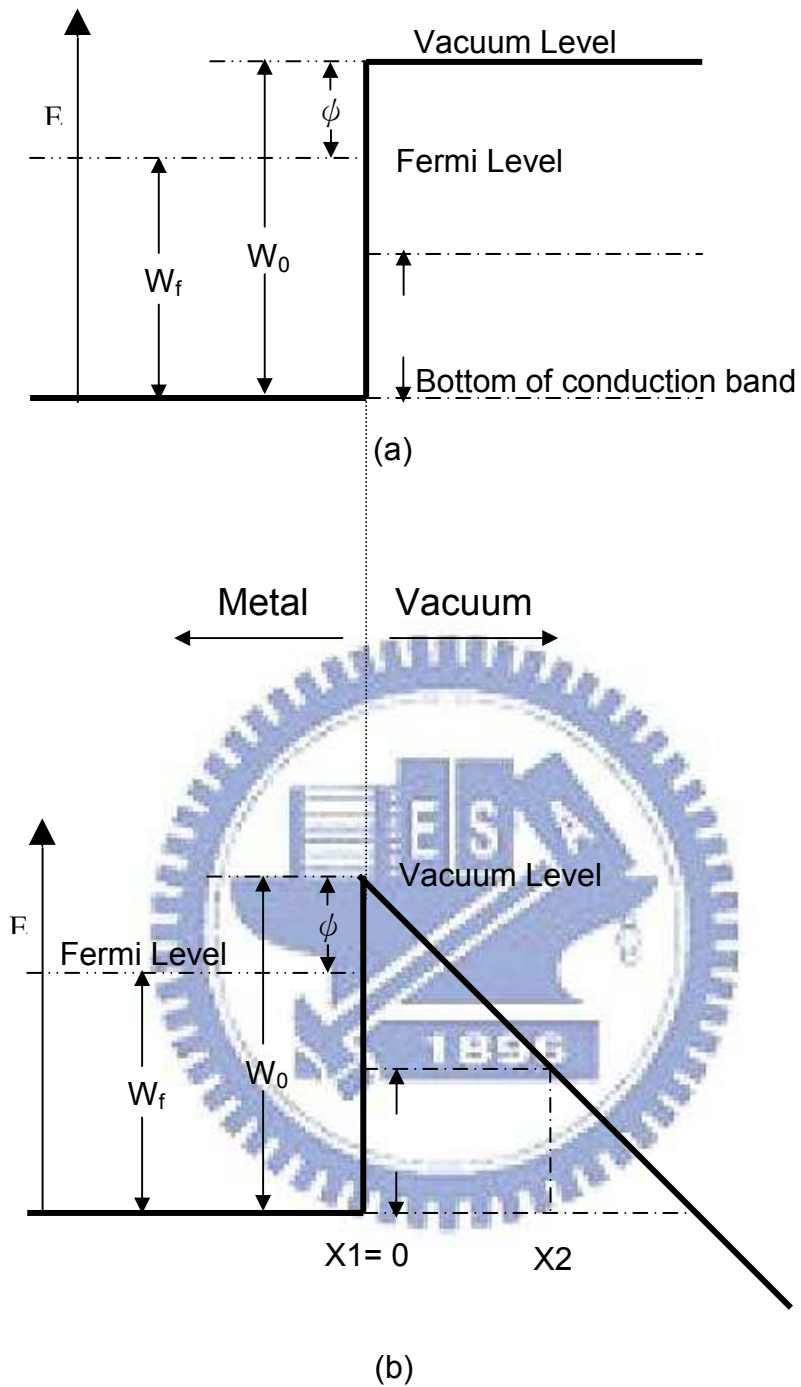


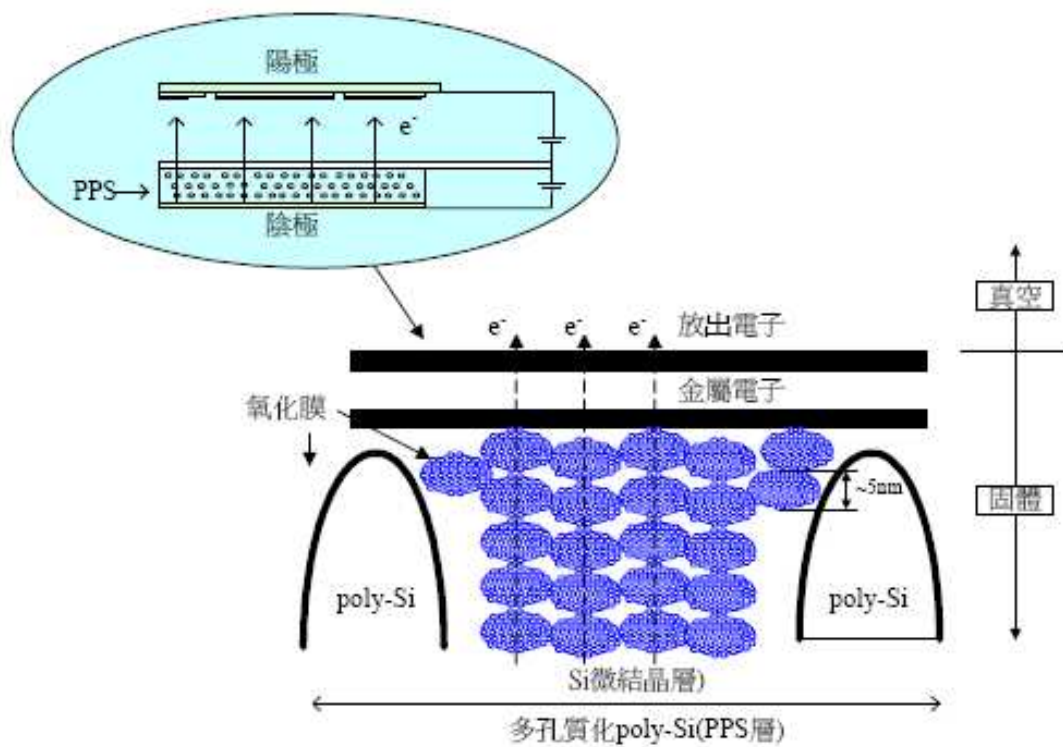
Figure 1-3 Energy diagrams of vacuum-metal boundary:

(a) without external electric field;

(b) with an external electric field.

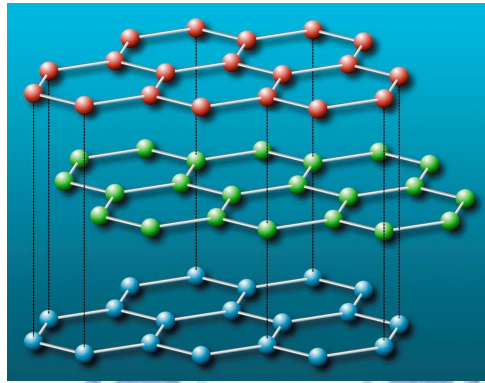


Figure 1-4 The full color FED products: (a) Pixtech 5.6" color FED based on Spindt-type, (b) Futaba 7" color FED based on Spindt-type, (c) Sony/Candescent 13.2" color FED based on Spindt-type, (d) Canon-Toshiba 36" SED-TV.

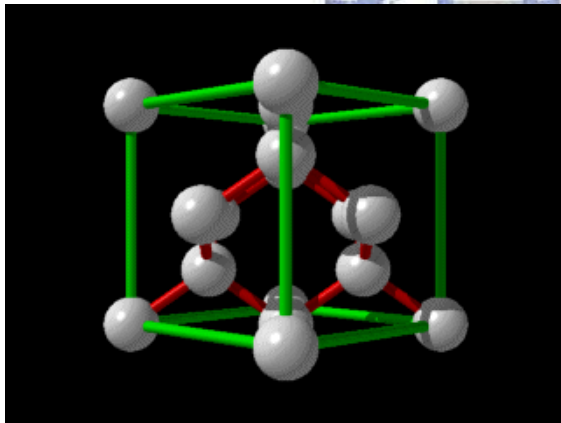


資料來源：Toray Research Center / PIDA 重製

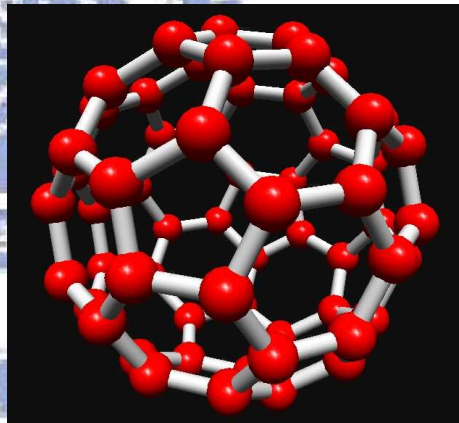
Figure 1-5 This diagram is the field emission mechanism of BSD.



(a)



(b)



(c)

Figure 1-6 Structures of carbon (a) graphite, (b) diamond, (c) fullerene

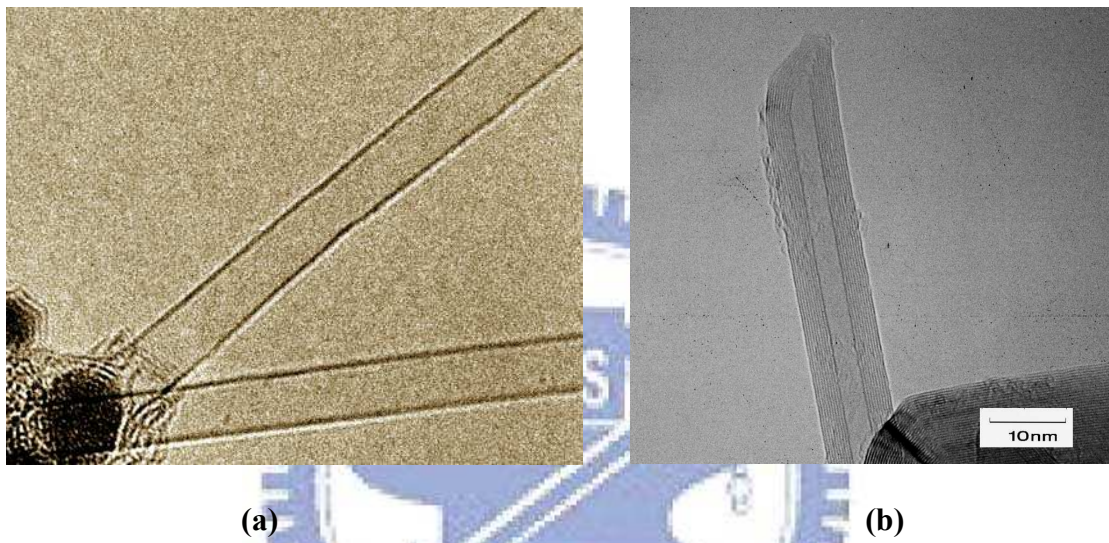
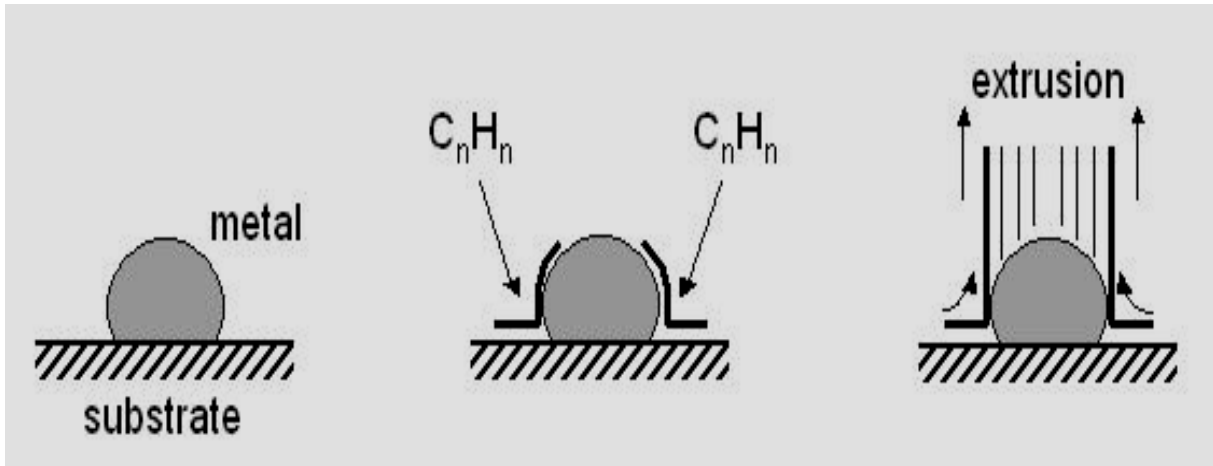
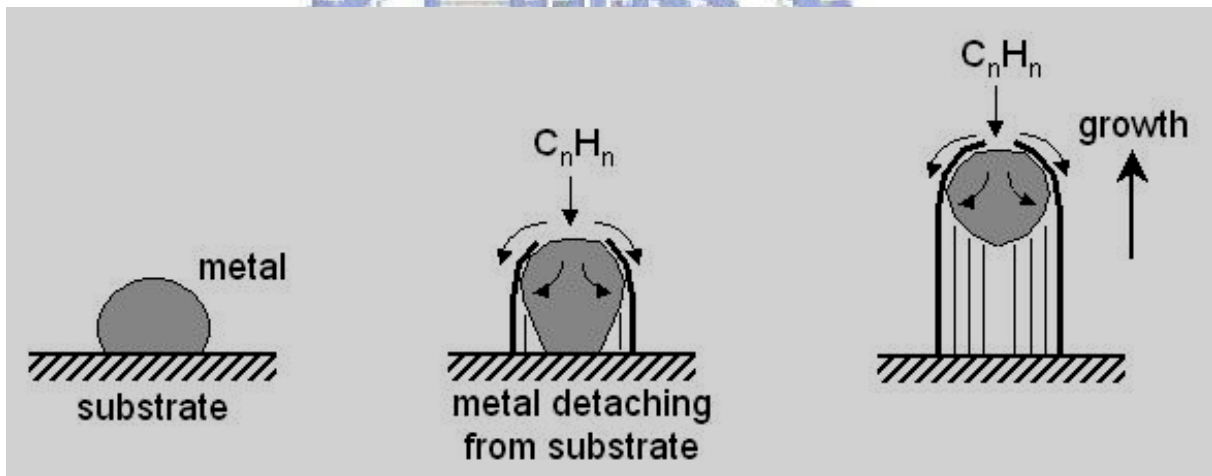


Figure 1-7 TEM images of (a) SWNT, and (b) MWNT



(a)



(b)

Figure 1-8 Growth mechanism of CNTs growth (a) base growth model, (b) tip growth model

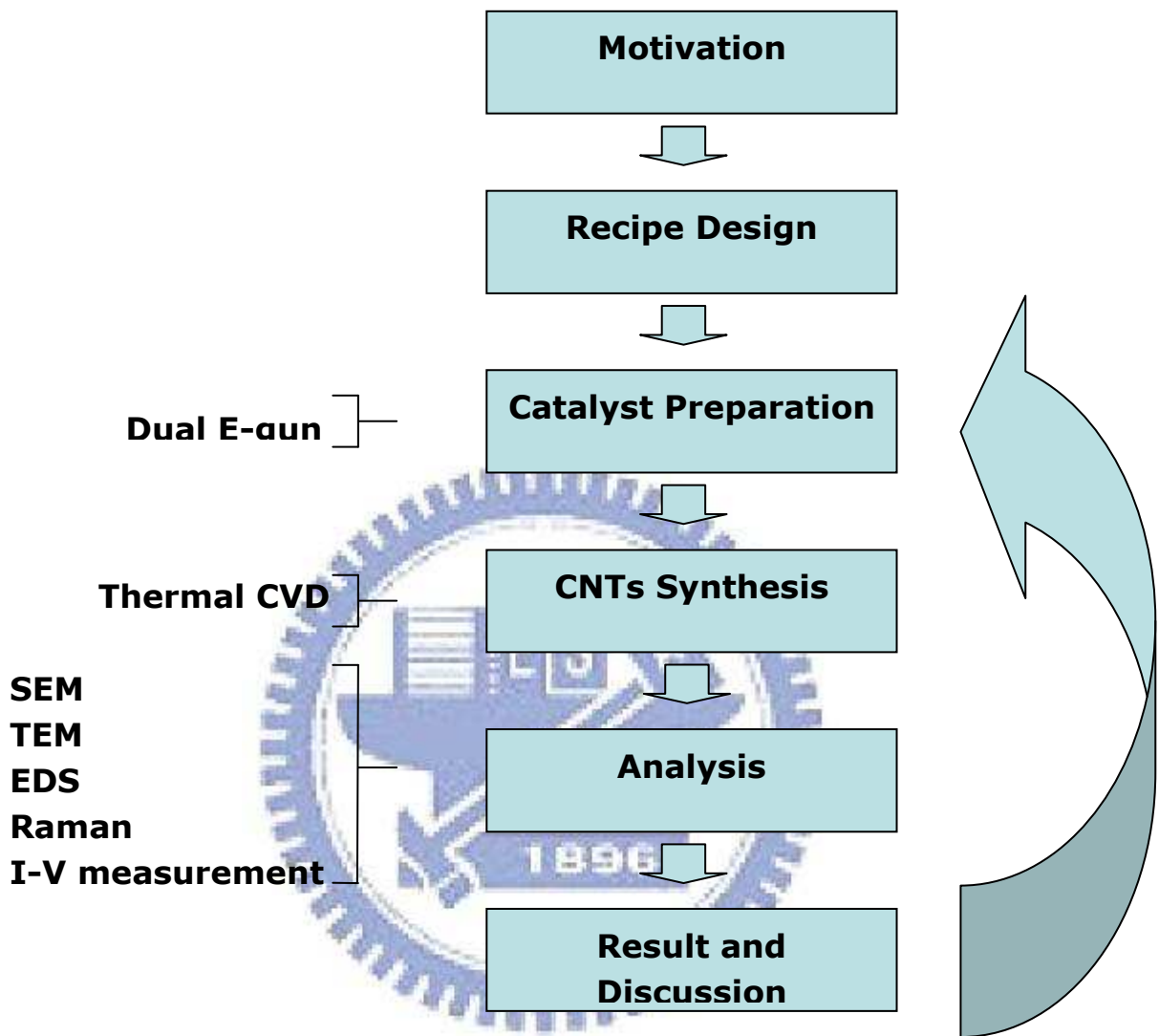


Figure 2-1 experiment procedures



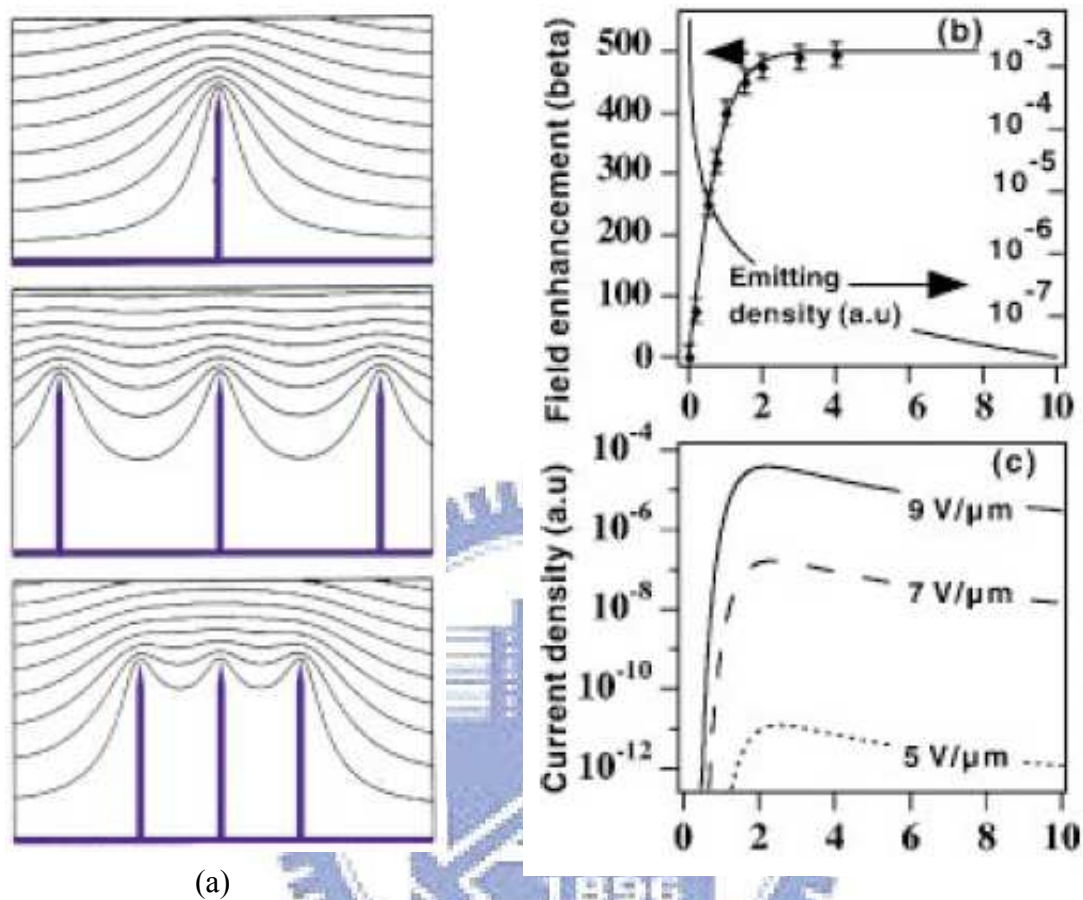


Figure 2-2 (a) Simulation of the equipotential lines of the electrostatic field for tubes of 1  $\mu\text{m}$  height and 2 nm radius, for distances between tubes of 4, 1, and 0.5  $\mu\text{m}$ ; along with the corresponding changes of the field enhancement factor  $\beta$  and emitter density (b), and current density (c) as a function of the distance.

(Ref. Appl. Phys. Lett. 76 (2000) 2071)

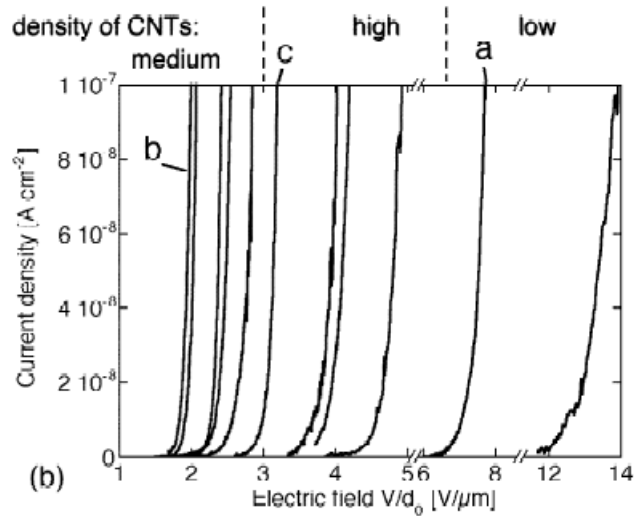
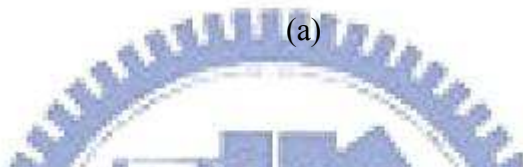
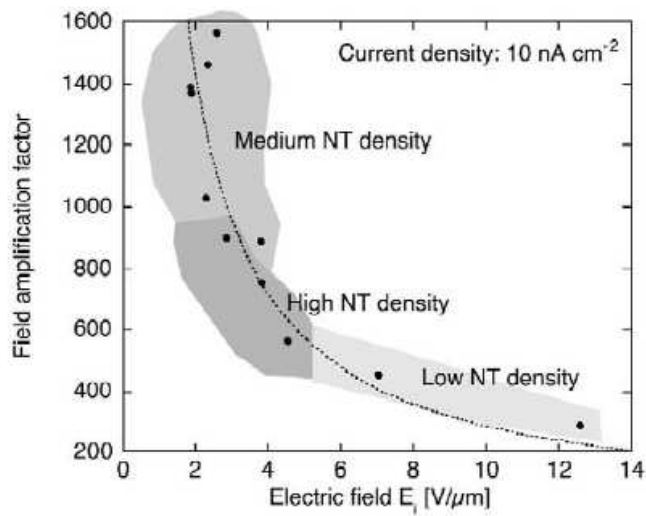


Figure 2-3 (a) Field amplification factor  $\beta$  as a function of the onset field after training,  $E_i$ , for the films obtained by CVD with different catalyst concentrations. (b) Low current field emission characteristics of the 11 samples after training. (Ref. Carbon 40 (2002) 1715)

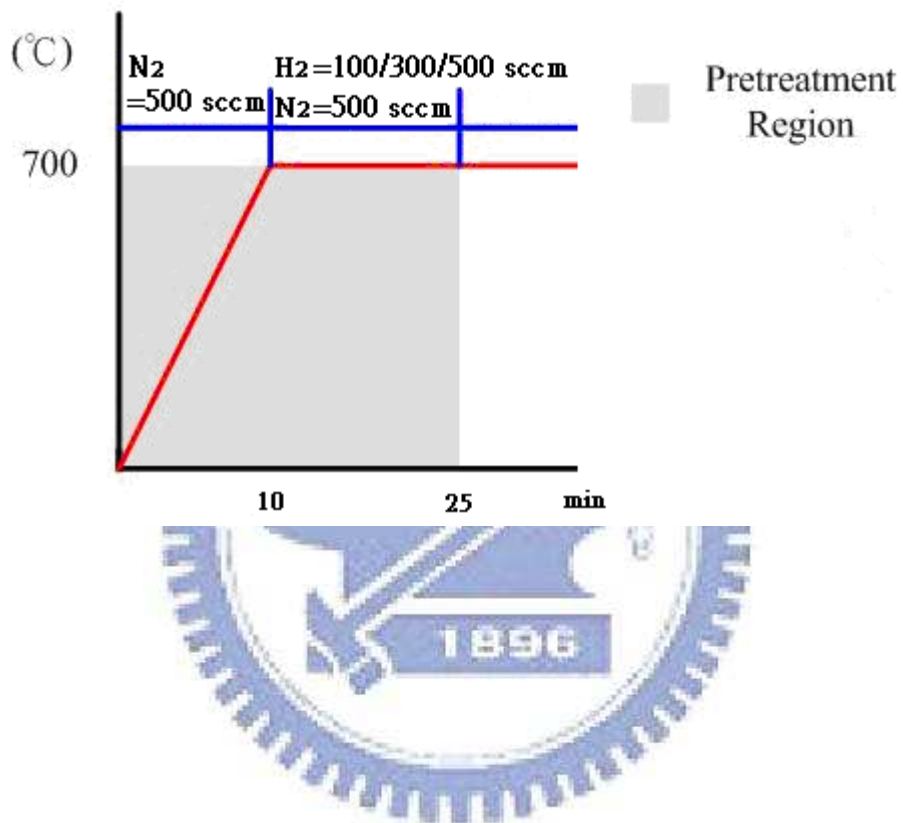


Figure 2-4 Growth condition of CNT pillars in the thermal CVD system.

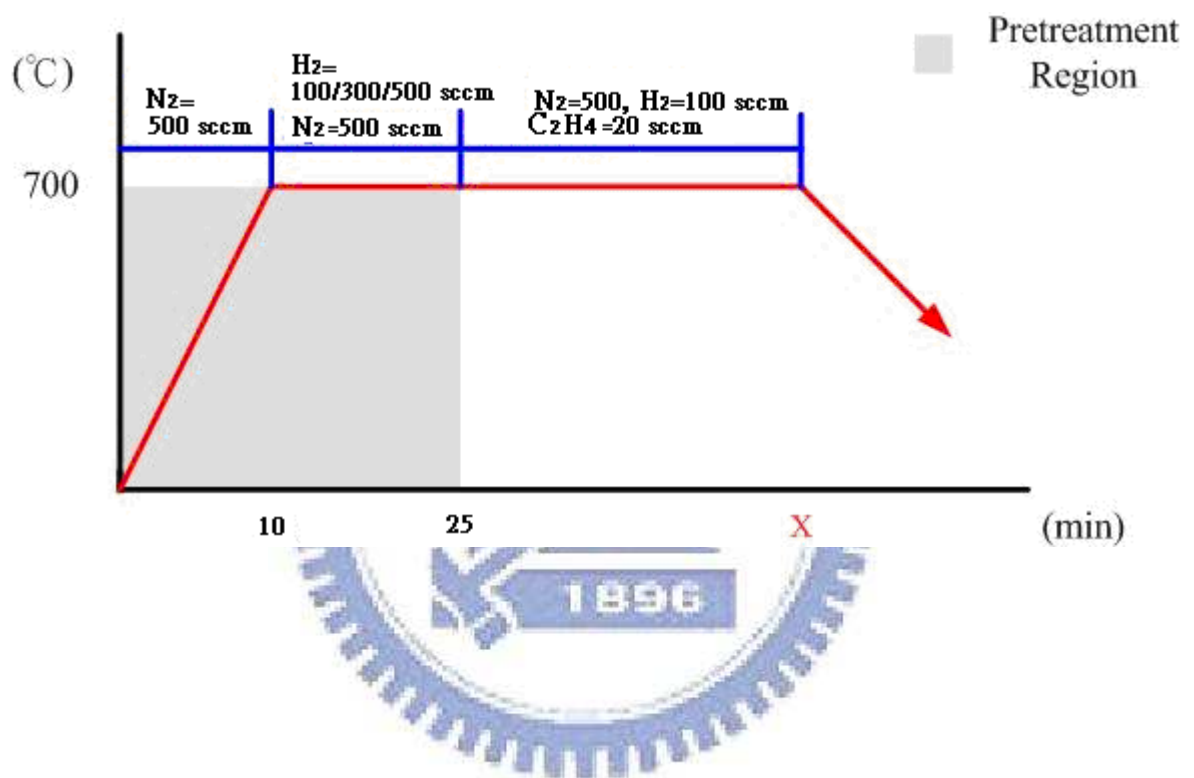


Figure 2-5 Growth condition of CNT pillars in the thermal CVD system.

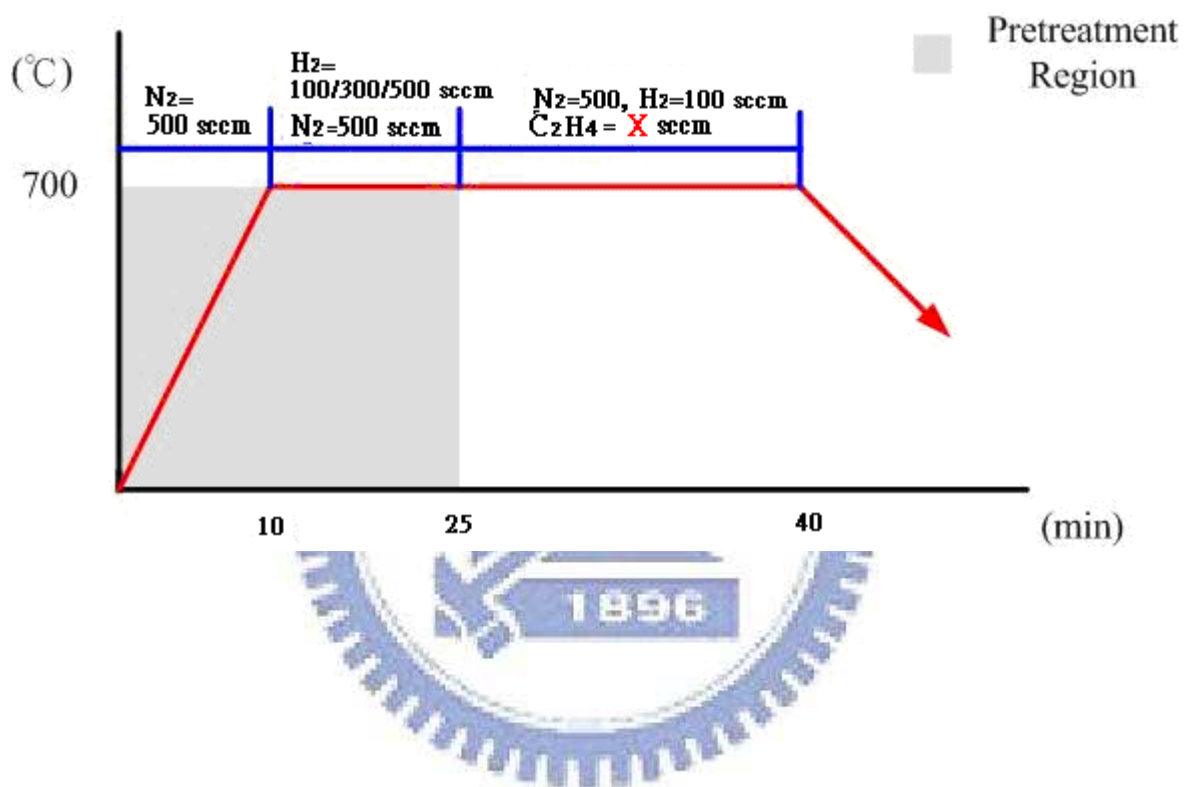


Figure 2-6 Growth condition of CNT pillars in the thermal CVD system.

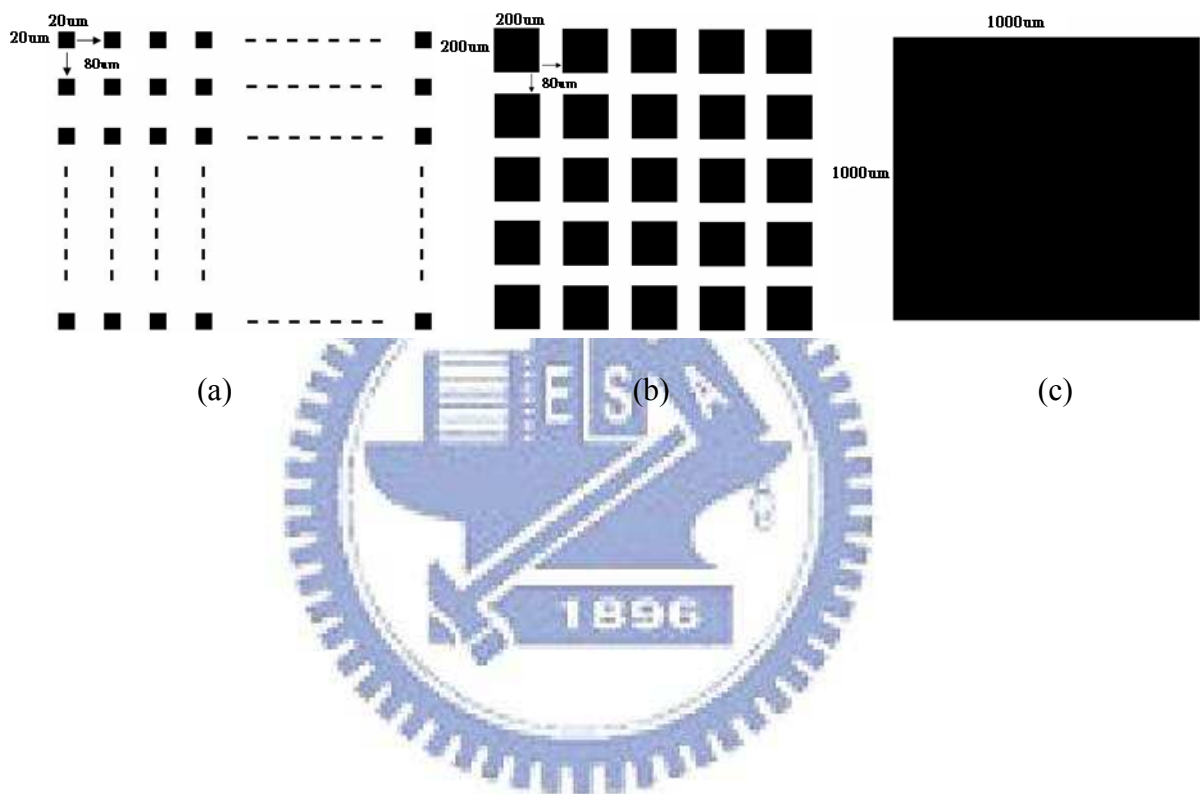
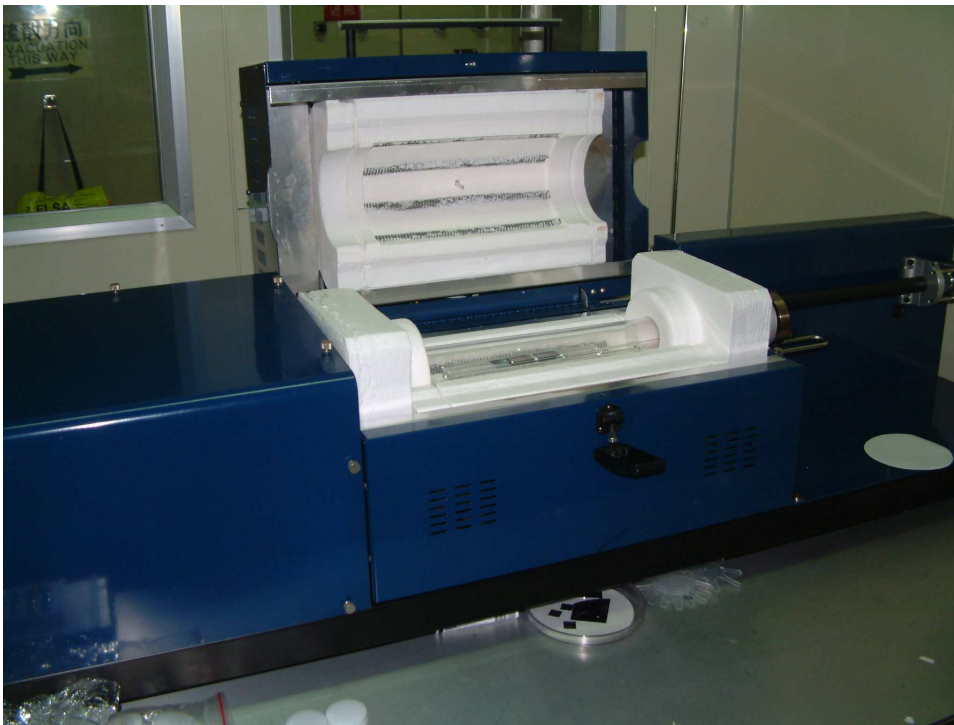
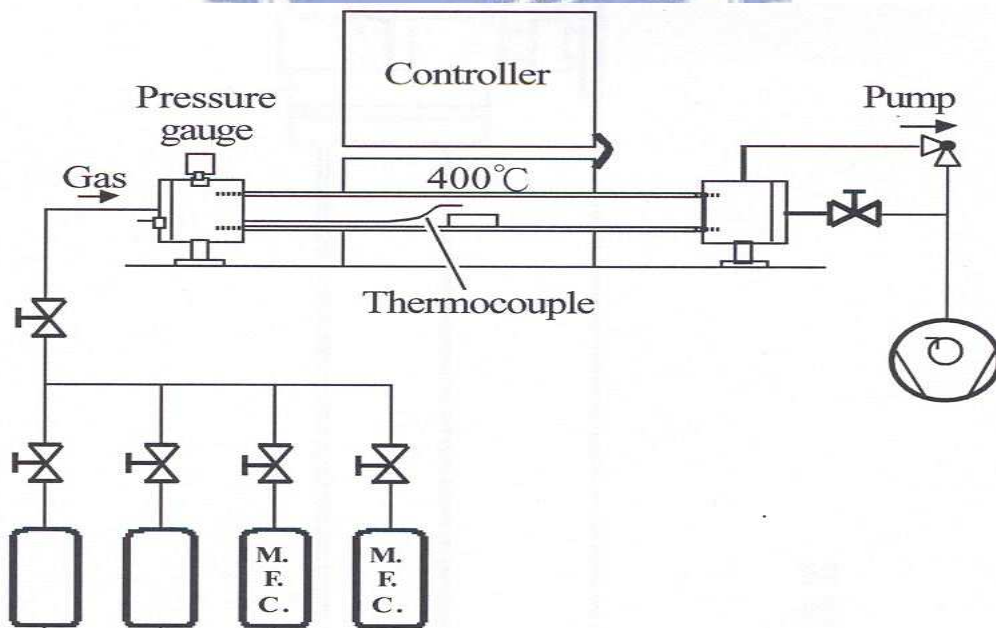


Figure 2-7 (a) Emission Area:  $20 \times 20 \times 50 \times 50 = 10^6 \mu\text{m}^2$  Perimeter:  $80 \times 2500 = 2 \times 10^5 \mu\text{m}$  (b) Emission Area:  $200 \times 200 \times 5 \times 5 = 10^6 \mu\text{m}^2$  Perimeter:  $800 \times 25 = 2 \times 10^4 \mu\text{m}$  (c) Emission Area:  $1000 \times 1000 = 10^6 \mu\text{m}^2$  Perimeter:  $4 \times 10^3 \mu\text{m}$ , the Perimeter ratios = 50 : 5 : 1



(a)



(b)

Figure 2-8 A (a) photo and (b) schematic picture of thermal CVD

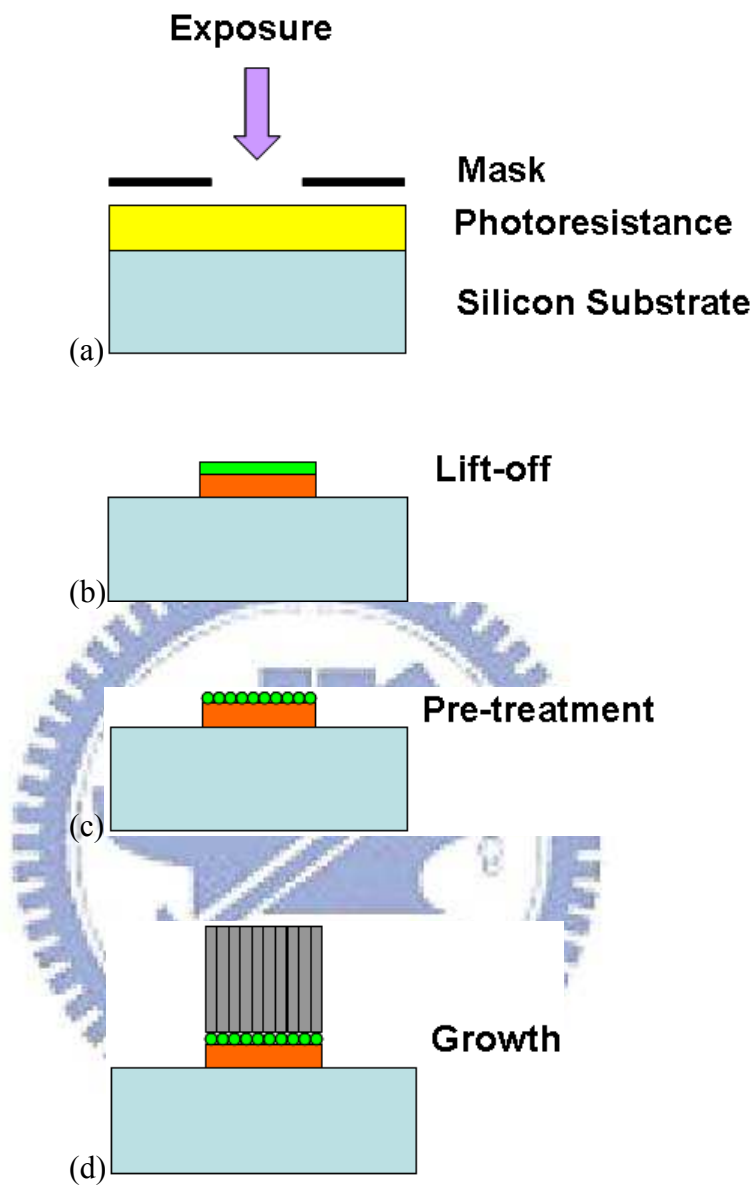
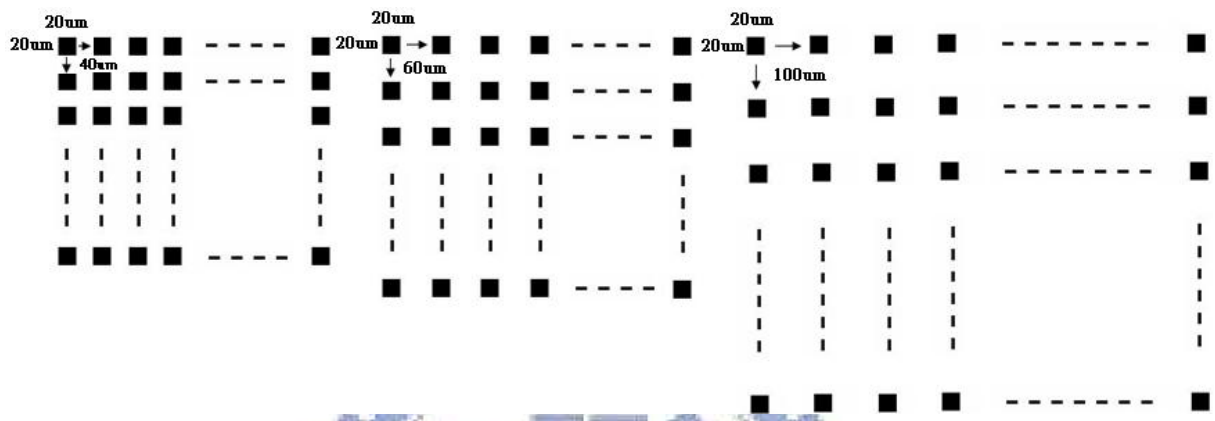


Figure 2-9 Experimental procedures for CNT pillars synthesized





(a)

(b)

(c)



Figure 2-10 (a)Pixel Area: $8.76 \times 10^6 \mu\text{m}^2$  (b)Pixel Area: $15.5 \times 10^6 \mu\text{m}^2$

(c)Pixel Area: $34.81 \times 10^6 \mu\text{m}^2$

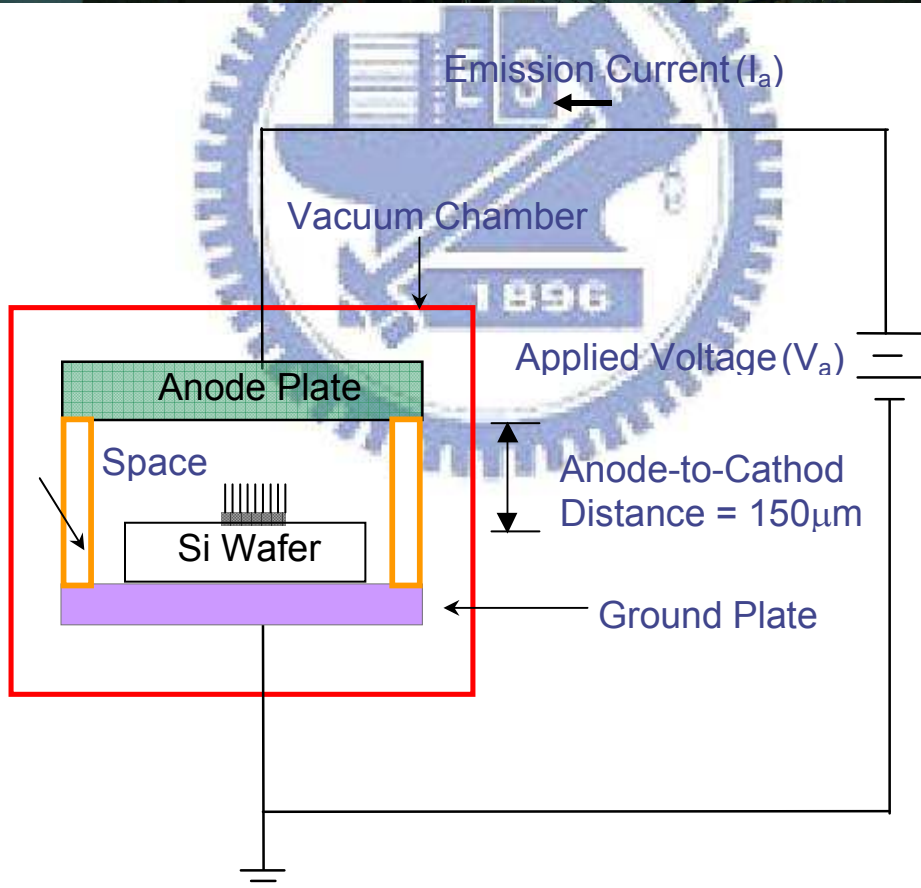
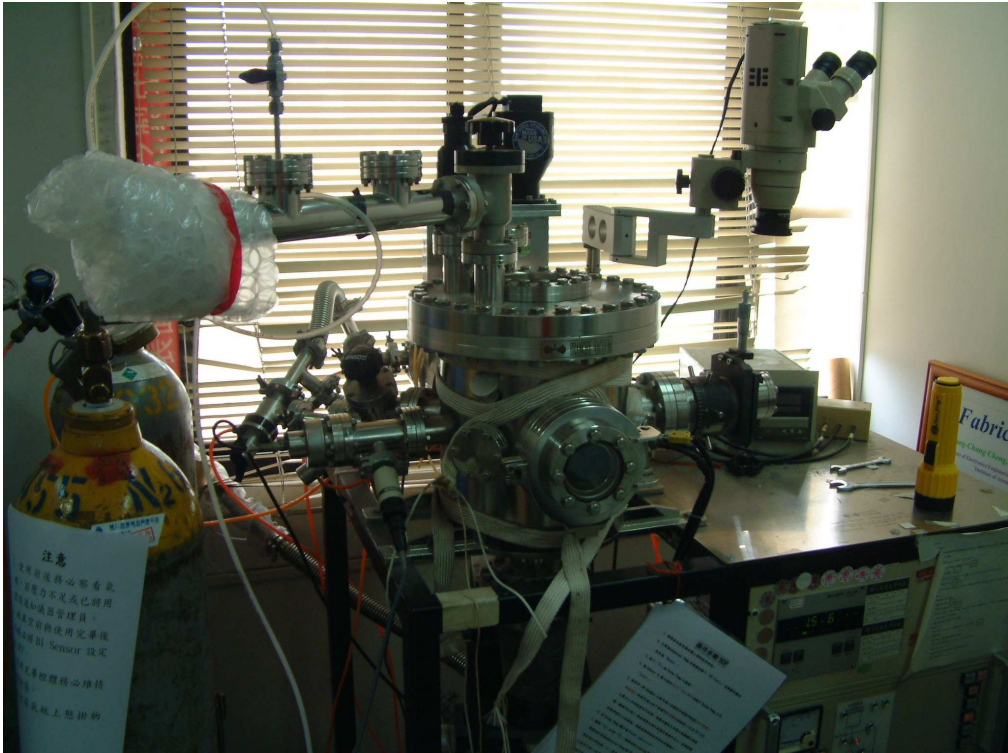
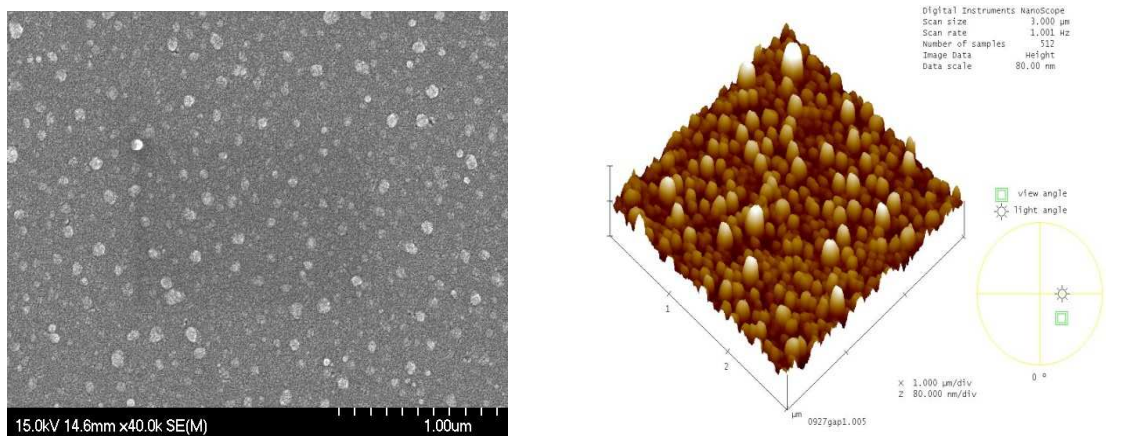
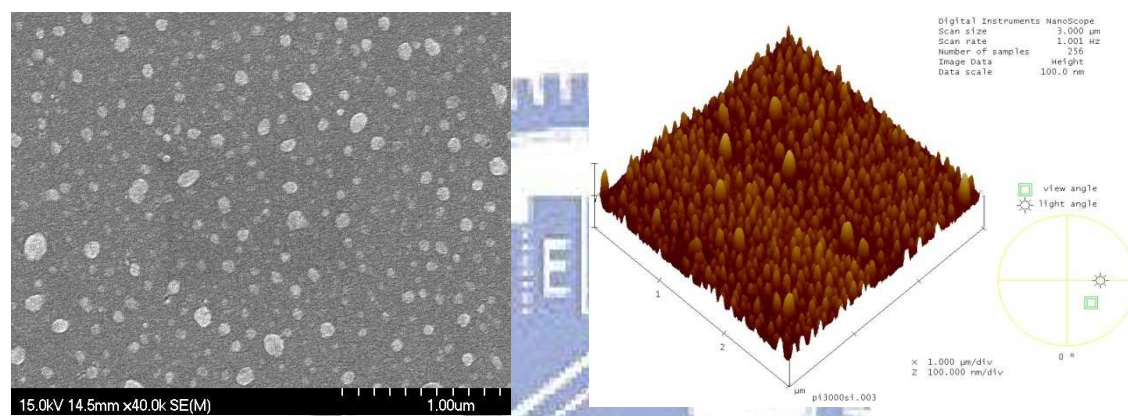


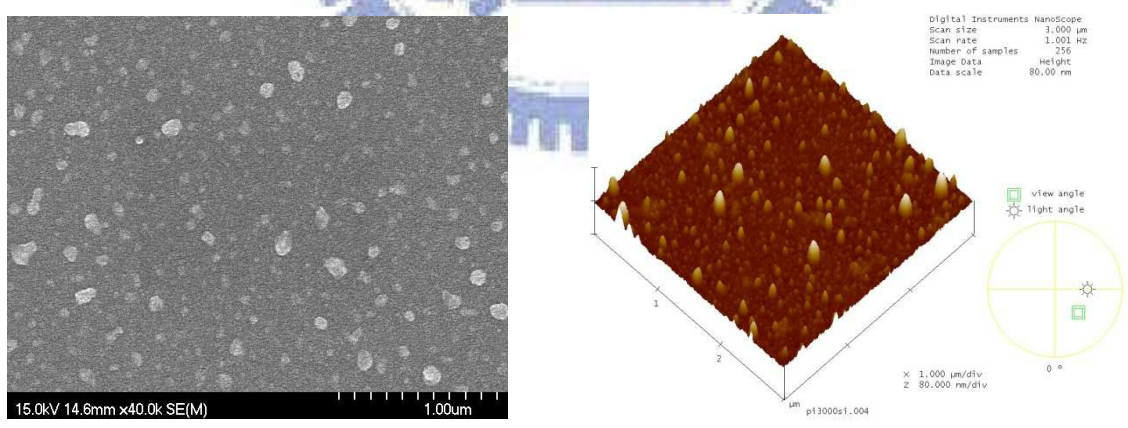
Figure 2-11 Schematic diagram of a high-vacuum system setup for field emission measurement.



( a ) N<sub>2</sub>/H<sub>2</sub>:500/100(sccm)

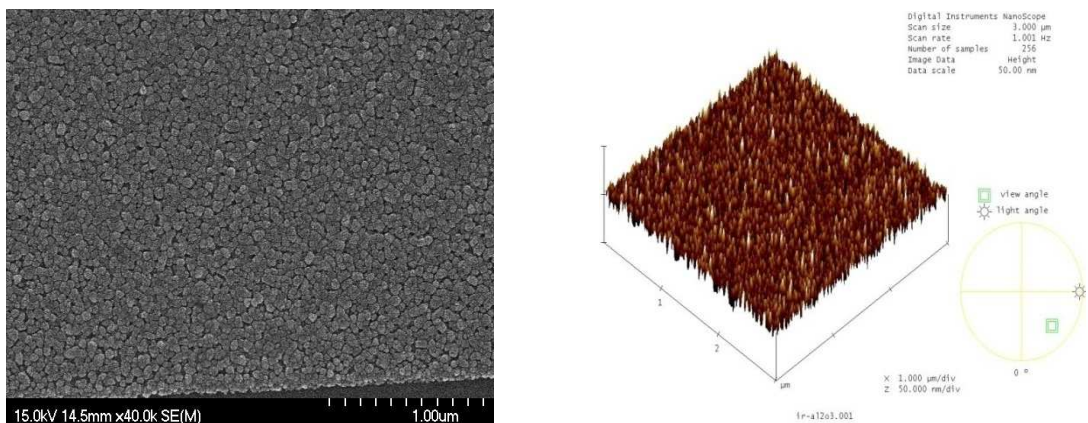


( b ) N<sub>2</sub>/H<sub>2</sub>:500/300(sccm)

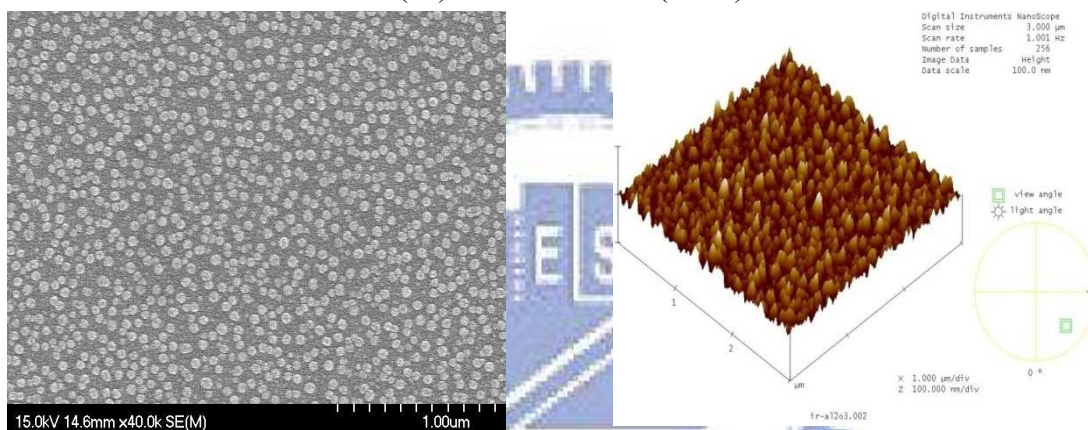


( c ) N<sub>2</sub>/H<sub>2</sub>:500/500(sccm)

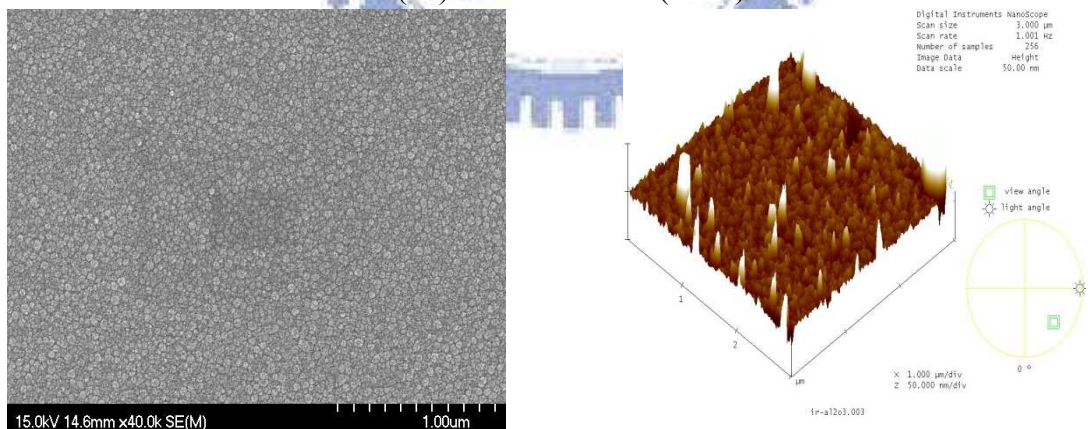
Figure 3-1 SEM and AFM micrographs of Ni /Ti bi-layered catalysts pre-treated in N<sub>2</sub>/H<sub>2</sub> gas mixtures with different hydrogen flow rates



( a ) N<sub>2</sub>/H<sub>2</sub>:500/100(sccm)

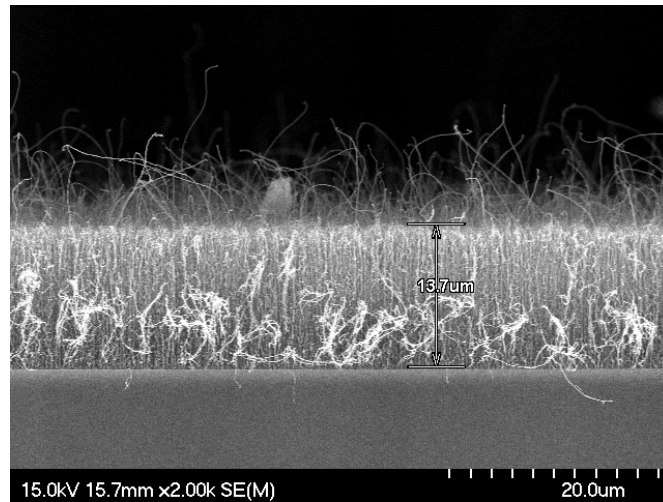


( b ) N<sub>2</sub>/H<sub>2</sub>:500/300(sccm)

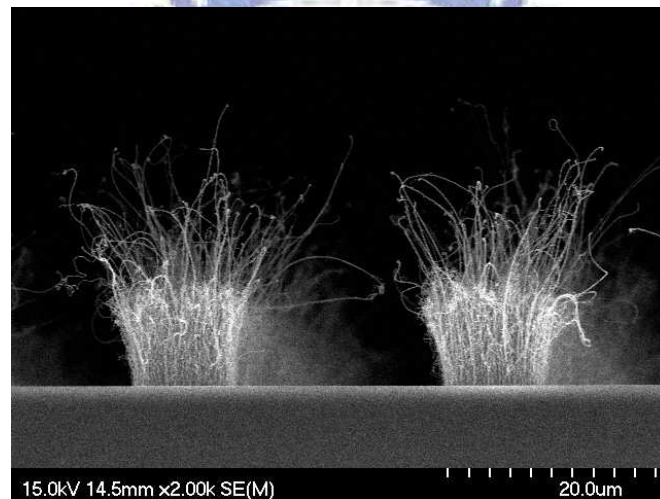


( c ) N<sub>2</sub>/H<sub>2</sub>:500/500(sccm)

Figure 3-2 SEM and AFM micrographs of Fe/Ti bi-layered catalysts pre-treated in N<sub>2</sub>/H<sub>2</sub> gas mixtures with different hydrogen flow rates



( a )

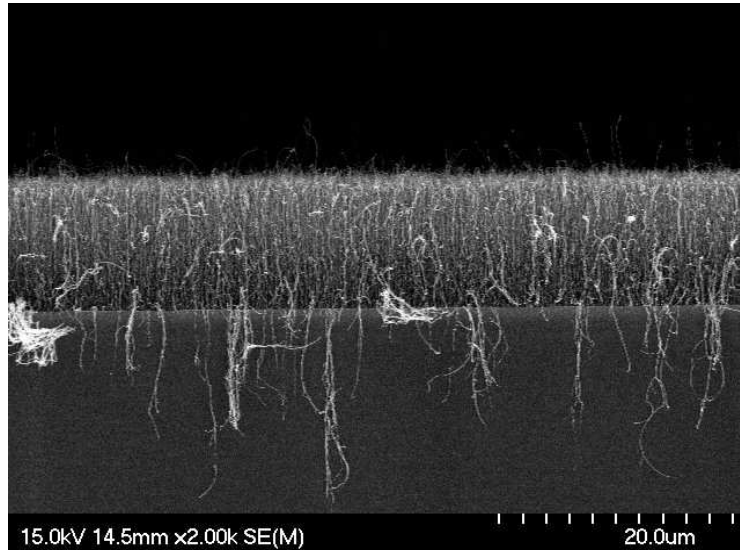


( b )

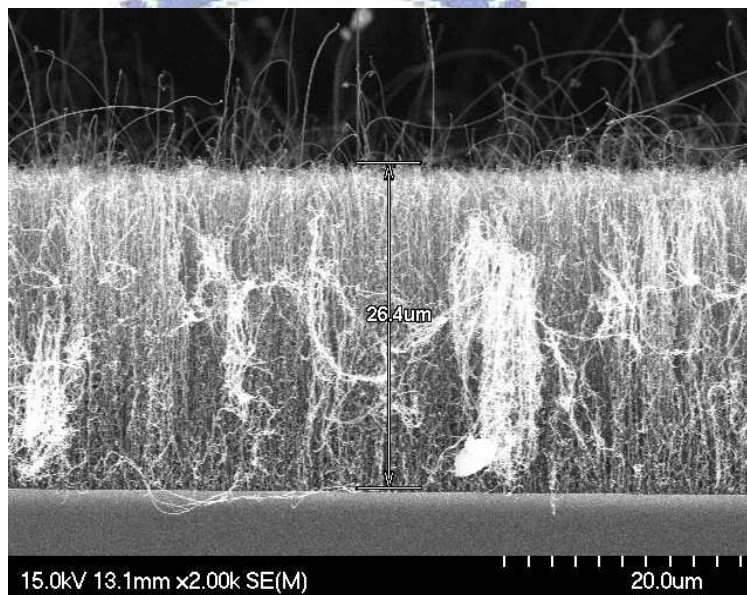
Figure 3-3 The typical SEM image using Fe/Ti bi-layered as catalysts for CNTs growth.

( a ) Growth condition: 700°C, Pretreatment: N<sub>2</sub>/H<sub>2</sub>=500/500, 15min, Growth: N<sub>2</sub>/H<sub>2</sub>/C<sub>2</sub>H<sub>4</sub>=500/0/40, 9min

( b ) Growth condition: 700°C Pretreatment:N<sub>2</sub>/H<sub>2</sub>=500/130, 15min, Growth: N<sub>2</sub>/H<sub>2</sub>/C<sub>2</sub>H<sub>4</sub>=500/100/20, 15min

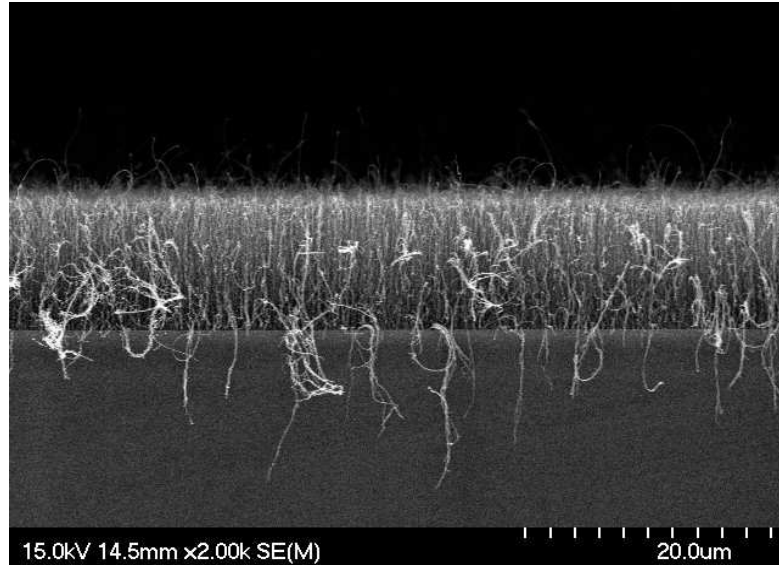


(a)

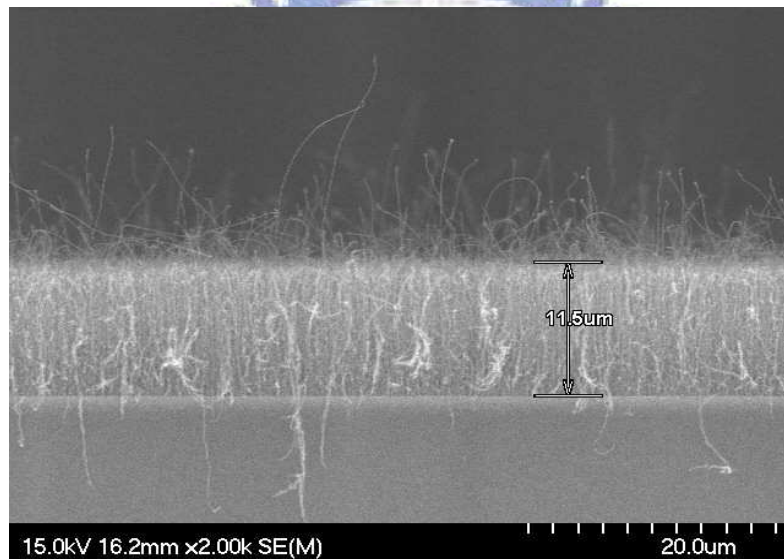


(b)

Figure 3-4 Effect of Growth time on the morphology of CNTs grown by Fe/Ti catalyst (a) 15min (b) 45min,  
 Growth condition: 700°C,  
 Pretreatment: N<sub>2</sub>/H<sub>2</sub>=500/100,15min,  
 Growth: N<sub>2</sub>/H<sub>2</sub>/C<sub>2</sub>H<sub>4</sub>=500/100/20



( a )



( b )

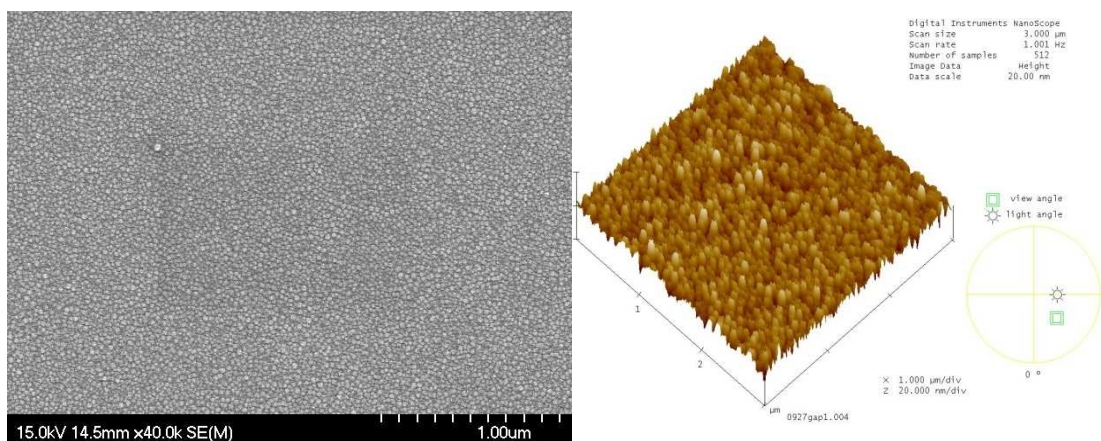
Figure 3-5 Effect of carbon source on the morphology of CNTs grown by

Fe/Ti catalyst. Growth condition : 700°C ,

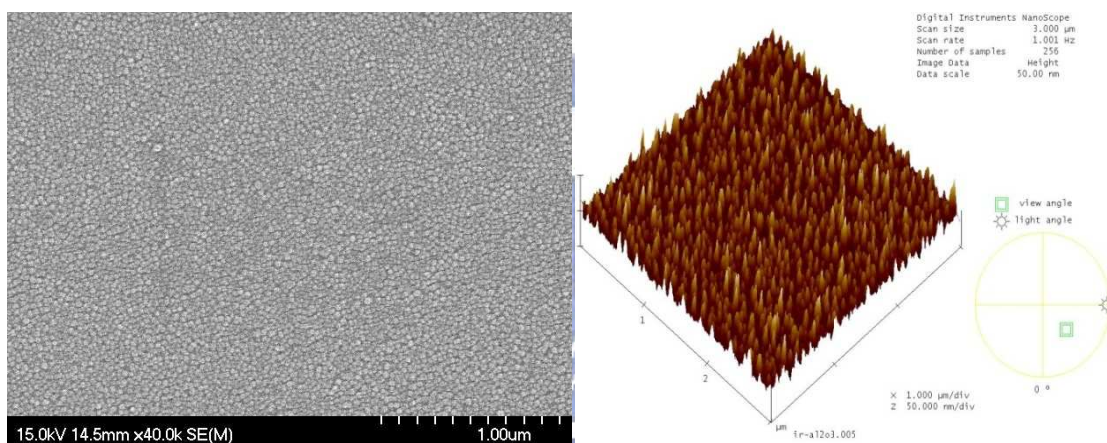
Pretreatment: N<sub>2</sub>/H<sub>2</sub>=500/100,15min,

Growth: (a)N<sub>2</sub>/H<sub>2</sub>/C<sub>2</sub>H<sub>4</sub>=500/100/20

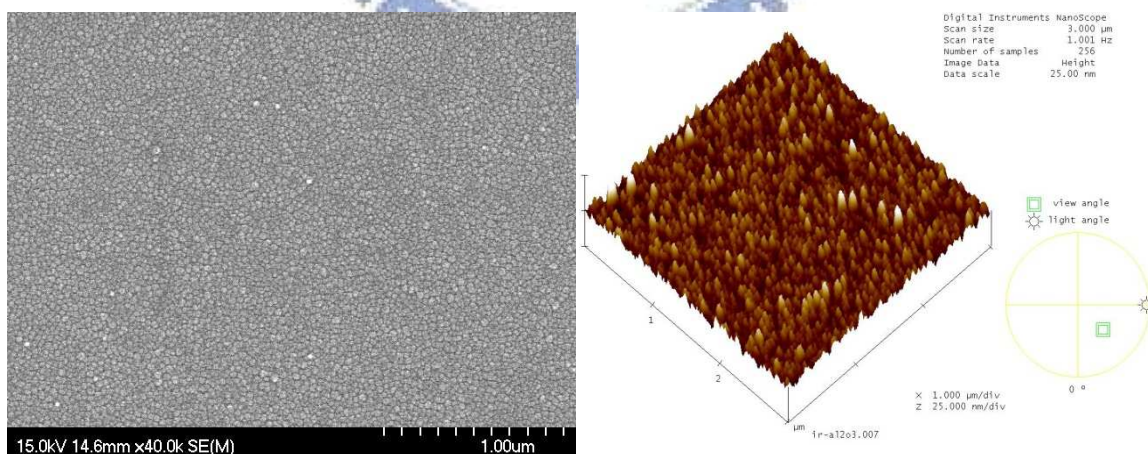
(b) N<sub>2</sub>/H<sub>2</sub>/C<sub>2</sub>H<sub>4</sub>=500/100/40



( a ) N<sub>2</sub>/H<sub>2</sub>:500/100(sccm)



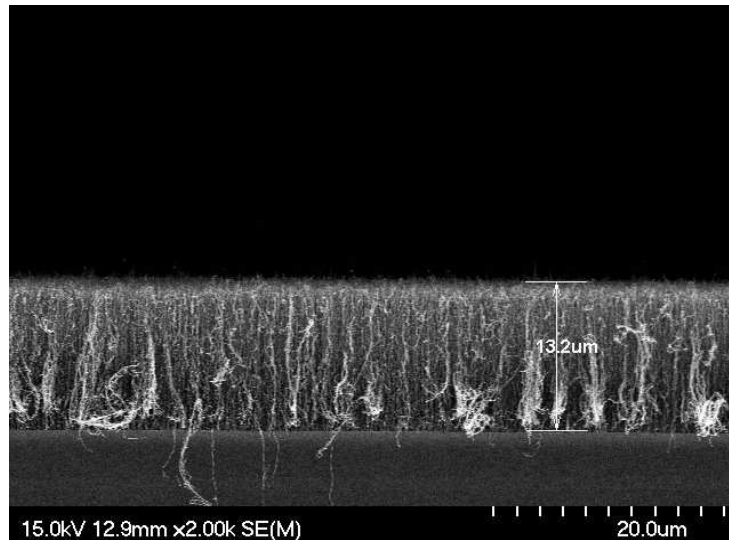
( b ) N<sub>2</sub>/H<sub>2</sub>:500/300(sccm)



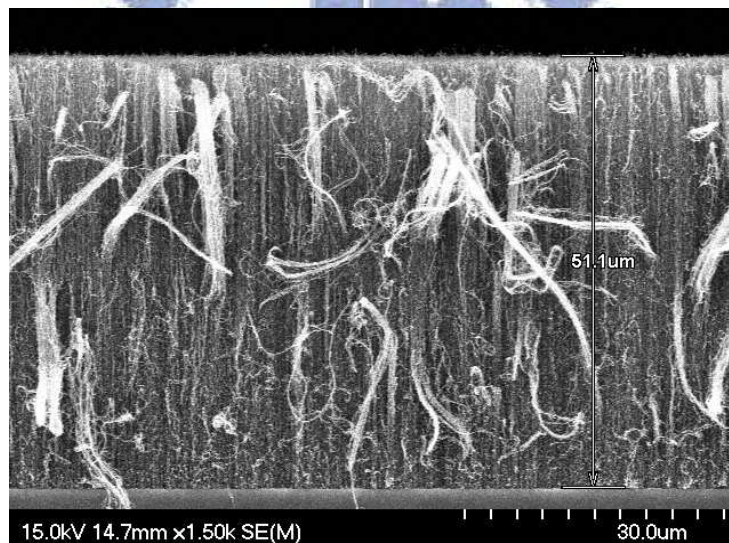
( c ) N<sub>2</sub>/H<sub>2</sub>:500/500(sccm)

Figure 3-6 SEM and AFM micrographs of Co /Ti bi-layered catalysts pre-treated in N<sub>2</sub>/H<sub>2</sub> gas mixtures with different hydrogen flow rates





( a )



( b )

Figure 3-7 Effect of growth time on the morphology of CNTs grown by Co/Ti catalyst (a) 15min (b) 45min, Growth condition: 700°C, Pretreatment: N<sub>2</sub>/H<sub>2</sub>=500/100, 15min, Growth: N<sub>2</sub>/H<sub>2</sub>/C<sub>2</sub>H<sub>4</sub>=500/100/20

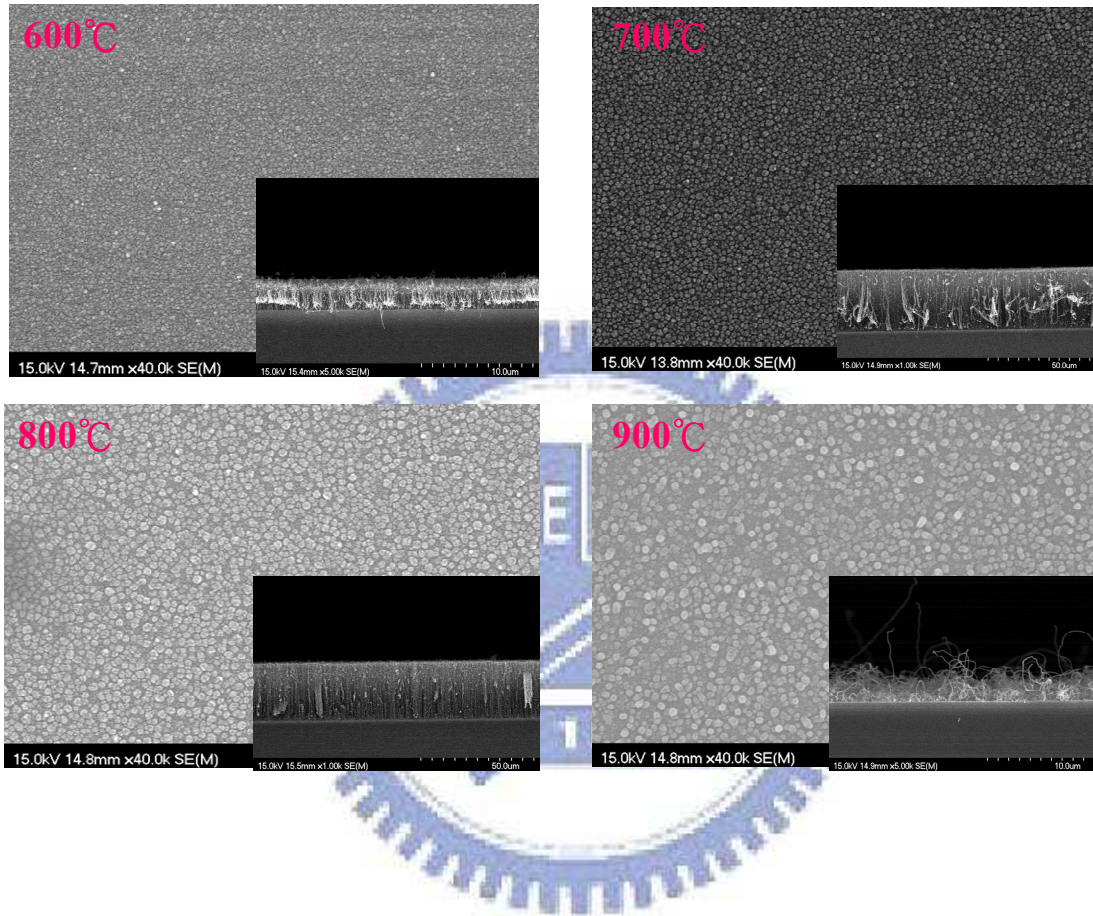
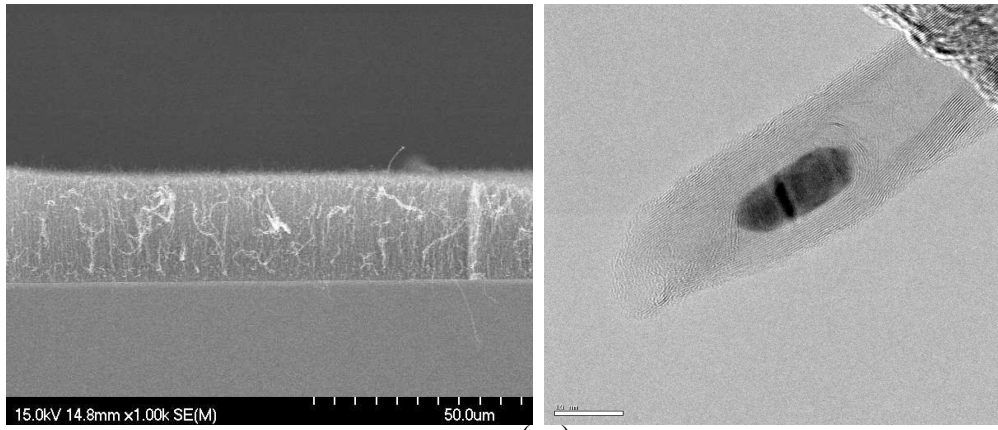
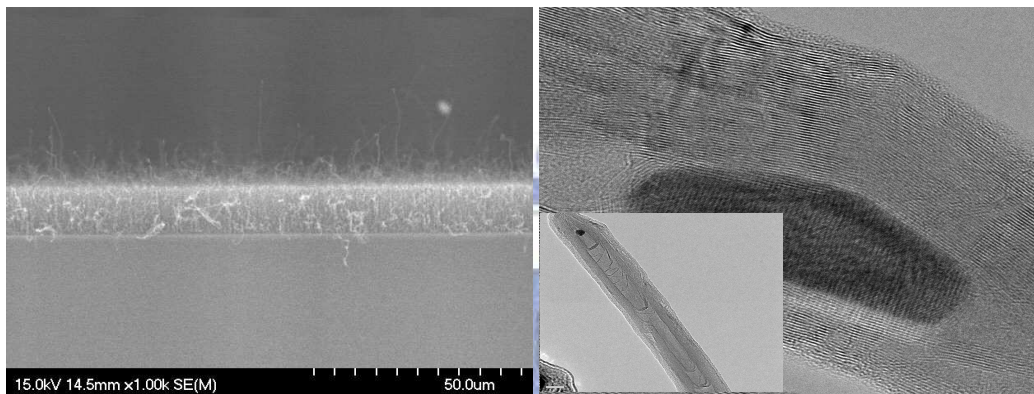


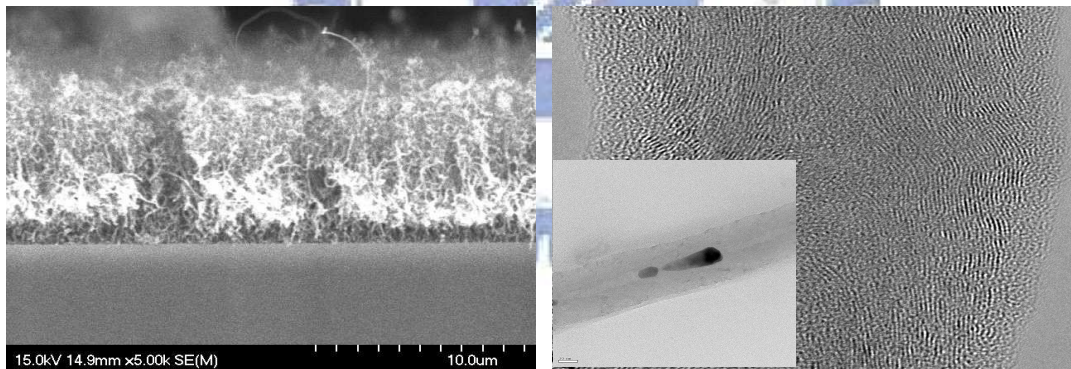
Figure 3-8 SEM micrographs of Co /Ti bi-layered catalysts pre-treated in  $N_2/H_2$  gas mixtures with different growth temperatures and their morphology of CNTs.



(a)

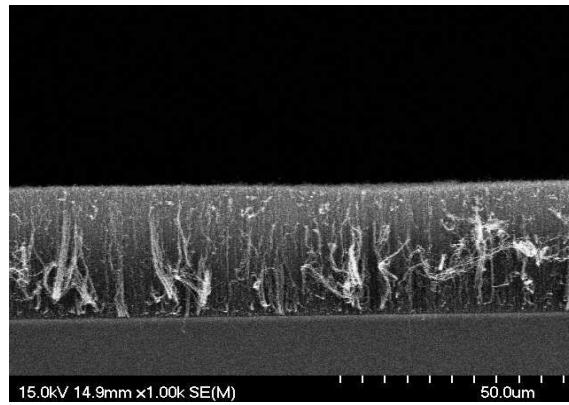


(b)

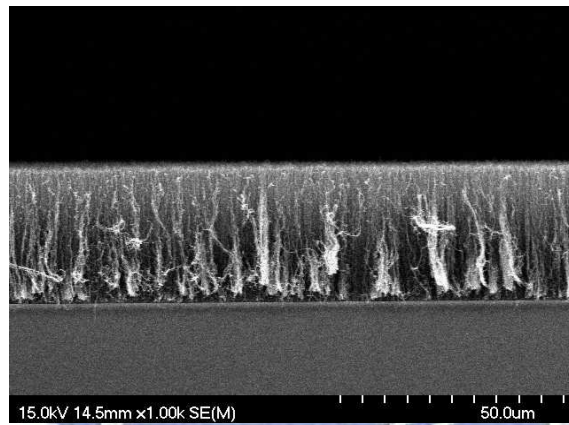


(c)

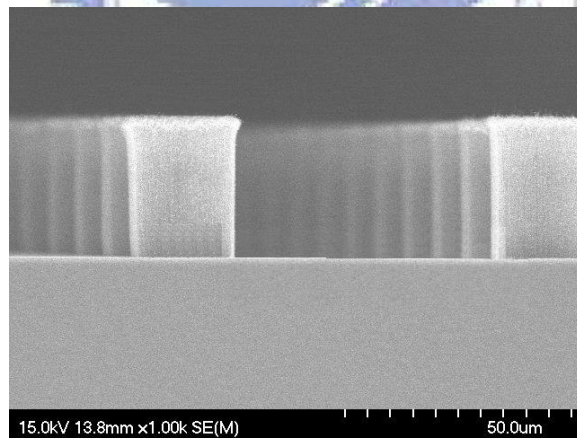
Figure 3-9 SEM and TEM micrographs of CNTs grown using (a) Co/Ti (b) Fe/Ti (c) Ni/Ti bi-layered catalyst



( a )



( b )



( c )

Figure 3-10 SEM micrographs of small, middle, and large sizes of CNTs' pixel arrays.

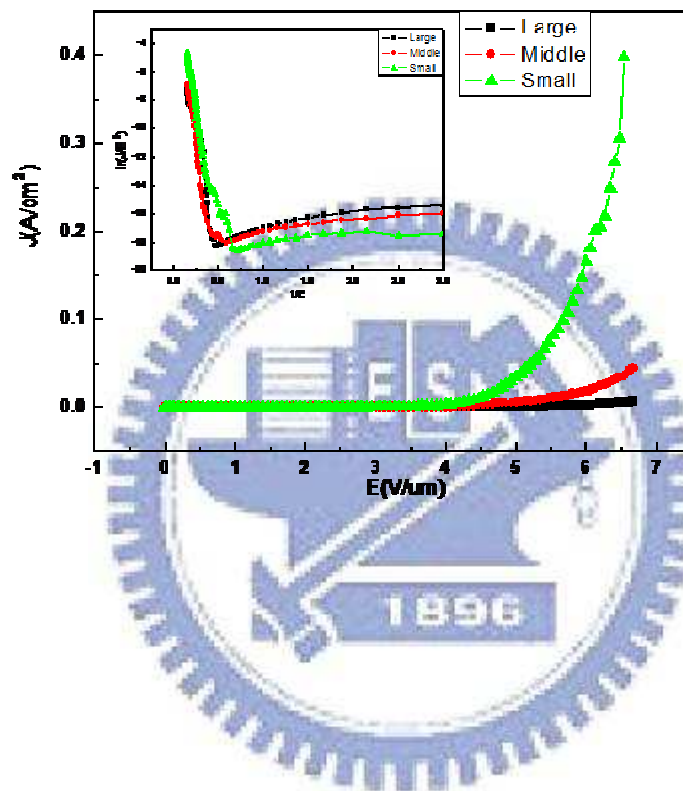


Figure 3-11 Field emission characteristics for small, middle, and large sizes of CNTs' arrays.